

## Research Paper

# A coupled multilevel vial lyophilization model for the pressure coupling in a freeze dryer

Blaž Kamenik , Jure Ravnik , Timi Gomboc, Matej Zadavec , Matjaž Hriberšek 

University of Maribor, Faculty of Mechanical Engineering, Smetanova ulica 17, SI 2000, Maribor, Slovenia

## ARTICLE INFO

## Keywords:

Freeze-drying  
Lyophilization  
Conjugate heat and mass transfer  
Computational fluid dynamics  
Multi-scale modeling

## ABSTRACT

With computational modeling of lyophilization in vials, the pressure coupling between the sublimation front and the drying chamber has traditionally been calculated using a simplified mass transfer resistance model in the form of a  $R_p$  model, which takes into account the headspace and the stopper in a simplified way. In developing a 3D CFD-based digital twin of lyophilization in vials, a need arises for a mass flow rate-dependent vial headspace/stopper model, as it enables a more accurate calculation of the pressure conditions above the shelf as well as pressure conditions directly at the sublimation front, the latter directly affecting the sublimation mass transfer rate as well as the temperature inside the product, which is crucial for determining the risk of product collapse. The local pressure variations at a shelf level affect the heat transfer conditions due to heat conduction in the low pressure environment of the drying chamber. In the present work the development of a coupled multilevel vial lyophilization model for the freeze-drying of vials is reported, with the time-dependent 1D heat and mass transfer model at the vial level coupled with the time-dependent 3D low-pressure CFD model of the flow of the water vapor–air mixture in the drying chamber heated by the shelves. A direct pressure coupling between the sublimation front and the drying chamber space in form of vial type specific headspace/stopper resistance model is implemented. The developed multilevel lyophilization model is used to study the pressure build-up above the shelf and the headspace of the vial and its influence on the product temperature at the bottom of the vial using simulations carried out for different chamber pressures (6 Pa and 22 Pa), shelf temperatures ( $-20\text{ }^{\circ}\text{C}$  and  $+10\text{ }^{\circ}\text{C}$ ) and vial types (10R and 15R). By implementing previously developed vial headspace/stopper pressure resistance models, the computational results show that the pressure build-up above the shelf and vial headspace significantly affect the product temperature at the bottom of the vial, especially at low chamber pressures ( $\leq 6\text{ Pa}$ ) and small gap sizes between the rubber stopper and the shelf above it. The increased pressure outside the vial leads also to higher heat transfer by conduction, which is particularly pronounced at the central shelf positions and within smaller shelf gaps. These results underline the importance of using a coupled multilevel model when analyzing the relationship between the local pressure variations above the shelf and their direct influence on product drying conditions, further improving the predictive capabilities of CFD based multilevel lyophilization models, especially with respect to detecting the product collapse temperature.

## 1. Introduction

Freeze-drying, or lyophilization, is a widely used dehydration process in pharmaceutical manufacturing, particularly for preserving biopharmaceuticals, vaccines, and other heat-sensitive formulations. Unlike conventional drying, lyophilization takes place at low temperatures, ensuring that product stability is maintained while extending shelf life. The process consists of three distinct phases: freezing, primary drying, and secondary drying. Initially, the aqueous solution containing the active ingredient is frozen at atmospheric pressure, forming ice crystals [1]. In the primary drying phase, the system pressure is

reduced while heat is gradually supplied via heated shelves to promote sublimation of the ice. Once all the ice has been sublimated, secondary drying commences, wherein residual moisture is removed by further increasing the shelf temperature to facilitate desorption. This step is crucial to achieving the desired moisture content for long-term product stability.

Mathematical models of varying complexity have been developed to simulate the dynamic drying process within vials. These models range from simple zero-dimensional (0D) lumped models [2] to more detailed one-dimensional (1D) [3] and two-dimensional (2D) axisymmetric vial models [4,5]. The primary advantage of 0D models lies

\* Corresponding author.

E-mail address: [blaz.kamenik@um.si](mailto:blaz.kamenik@um.si) (B. Kamenik).

in their computational efficiency, making them ideal for parametric studies and initial process design. However, their simplifications limit their accuracy when scaling up to industrial applications. One of the main drawbacks of lyophilization is its inherently long drying times and high operational costs [6]. To mitigate these issues, more aggressive drying cycles have been explored to accelerate the process and reduce energy consumption [7]. The chamber pressure plays a key role in controlling the heat input to the drying product [2,8–10]. Increasing chamber pressure enhances heat transfer, leading to faster drying, but also introduces the risk of product collapse due to excessive thermal stress. Conversely, lower chamber pressures ensure structural integrity but at the expense of prolonged drying cycles. A critical limitation in aggressive drying cycles is the possibility of choked flow, where the sublimation rate increases to a point where the water vapor velocity reaches the speed of sound in the connecting duct. This phenomenon can lead to uncontrolled pressure increases and potential batch failure if the product temperature exceeds its collapse threshold.

Flow conditions within the lyophilizer significantly impact local drying kinetics, necessitating the use of computational fluid dynamics (CFD) to model the process. CFD simulations solve continuum-based transport equations (Navier–Stokes equations) and have demonstrated their accuracy in capturing flow behavior under rarefied conditions by appropriately modifying boundary conditions [11]. Commercial CFD codes have been extensively used to analyze choked flow [12,13] and optimize system performance by adjusting chamber pressure and shelf temperature. Additional research has investigated the influence of heterogeneous vapor–fluid dynamics within the drying chamber [14]. Factors such as pressure gradients along shelves, non-uniform shelf temperatures, and the introduction of inert gases have been shown to affect drying efficiency. Studies have also focused on modeling flow through the connecting duct between the drying chamber and the condenser [15–17], as well as pressure drop effects due to vial and stopper geometry [18] and stopper position [19]. Some studies [16,20] have modeled non-uniform freezing on condenser surfaces, while others [21] have incorporated deposition as a volumetric mass sink in CFD simulations. In [22] a mechanistic model that provides detailed insights into the kinetics of ice deposition during freeze-drying as a function of the condenser surface temperature was recently developed.

Another major challenge in lyophilization is scaling up from laboratory to production-scale freeze dryers. Differences in hydrodynamic conditions, heat transfer, and mass transfer characteristics make direct scale-up difficult. Studies have explored the effects of vial geometry and stopper design on pressure drop inside vials [2], highlighting the need for a comprehensive understanding of vial-specific resistance to sublimation flow. While prior CFD-lyophilization models [23,24] have successfully coupled 3D CFD simulations with quasi 1D vial drying models, pressure variations inside the vial-stopper interface remain poorly characterized. This work addresses this gap by developing a coupled CFD-1D model that integrates chamber flow dynamics with vial-scale mass transfer to accurately predict drying behavior at different scales.

## 2. Lyophilization in vials inside of drying chamber

During drying, the main driving force is the pressure difference between the vapor pressure at the sublimation surface and the chamber pressure. During sublimation, the process consumes heat, resulting in a drop in product temperature, which is prevented by supplying heat through heated shelves. To promote further drying, it is desirable to reach the highest allowable temperature of the product by increasing the temperature of the shelf, which increases the saturation pressure of the water vapor and thus increases the driving force for mass transfer. As the mass flow rate of the sublimate increases, this results in higher water vapor velocities inside the vial, which increases the pressure drop inside the vial. This leads to increased local pressure inside the vial (sublimation surface), which acts as an additional resistance for the

mass transfer [2,18]. On the other hand, the main mass transfer resistance occurs due to the formation of the dried porous cake that forms during drying of typical pharmaceutical solutions. As drying progresses, the height of the cake increases, resulting in higher resistance for mass transfer. When designing the scale-up procedure for lyophilization in vials, the focus is predominantly on the determination of the  $K_v$ , the heat transfer coefficient, and determination of the product mass flow resistance i.e.  $R_p$ . In the definition of the latter, typically the pressure difference between the sublimation front and the chamber pressure is used. This approach is straightforward to use, but the pressure difference, used in development of the  $R_p$  model, includes pressure drop not only due to the dried porous layer of the material, but also a non-negligible pressure drop contribution from the hydraulic resistance of the vial headspace, vial stopper as well as the local pressure increase across the shelves (due to the vapor flow). The classical way of defining the  $R_p$  is therefore applicable only for a selected combination of the product properties, vial geometry, stopper geometry and drying chamber geometry (clearance between the shelves).

### 2.1. Experimental study

Since the objective of this work is to evaluate the local pressure rise and the geometry of the drying chamber on the drying kinetics of the product inside the vial, specific experiments were performed to determine the sublimation kinetics. From the experimental results, in the form of time-dependent product temperature measurements or a combination of recorded temperatures and mass flow rates [25], model parameters for the numerical model are determined and used for validation of the numerical model.

#### 2.1.1. Materials

In the experiments, 10R borosilicate glass vials were used, having an outer diameter of 24 mm ( $d_o$ ), an inner diameter of 22 mm ( $d_i$ ), and an inner diameter of the vial neck of 12.6 mm. The height of the 10R vial is 45 mm and 52 mm with half inserted rubber stopper. 5% wt mannitol-water solution was used for all the experiments, which were performed in a Kambic LIO-2000 LFT [26] freeze dryer. To investigate the influence of the gap size on the pressure increase above the shelf, an additional numerical study was carried out with 15R vials, which have the same diameter as the 10R vials but a larger gap of 4.5 mm between the bottom of the vial and the top of the rubber stopper. No experiments were carried out with the 15R vials. The dryer has a separate drying chamber with two temperature-controlled stainless steel shelves, with a distance between the shelves of 71.5 mm, each with a shelf area of about 0.09 m<sup>2</sup> (width and length of 300 mm), and a condensation chamber with a condenser capacity of 5 kg. The pressure in the freeze dryer was monitored with the Pirani pressure gauge, which is also used to control the vacuum pump. However, instead of relying on its inefficient control loop, pressure regulation was managed manually. To improve pressure measurement, an additional capacitive manometer was installed on the existing system and connected to an external data acquisition system. The system pressure was set to the minimum attainable pressure, ensuring that the vacuum pump remained on. To maintain the desired pressure (as monitored by the capacitive manometer), nitrogen was introduced into the chamber, and the flow rate was manually adjusted using the bleed valve. Temperatures were measured using type *T* thermocouples that were 0.5 mm thick. Data were collected using the National Instrument NI cDAQ-9174 system.

#### 2.1.2. Experimental protocol

To validate the numerical model of drying of the product inside of the vial for a full freeze dryer, experiments were conducted with 10R vials. The purpose of the experiment was to determine the local drying kinetics for vials at different shelf locations. The vials were filled with 2 mL of mannitol-water solution. The thermocouples were positioned at the bottom of the vial (height =  $0.5 \pm 0.5$  mm), and 144 vials were

**Table 1**  
Freeze-drying cycles of 5% mannitol-water solution.

Protocol	Variable	Freezing	Primary drying	Secondary drying
P1	$T_{sh}$	-35 °C	-20 °C	+20 °C
	$p_c$	6 h	25 h	5 h
	Time		22 Pa	22 Pa
P2	$T_{sh}$	-35 °C	+10 °C	+20 °C
	Time	6 h	10 h	5 h
	$p_c$		22 Pa	22 Pa

loaded on each shelf (the bottom and upper shelf) of the freeze dryer. The freezing step lasted 6 h at the shelf temperature of -35 °C ( $T_{sh,f}$ ) and atmospheric pressure, then the chamber pressure was lowered and the shelf temperature was increased. Two sets of experiments were performed for each considered vial, at chamber pressure of 22 Pa and two different shelf temperatures. For the protocol P1, the shelf temperature was  $T_{sh,pd} = -20$  °C, for protocol P2  $T_{sh,pd} = +10$  °C, summarized in Table 1. Each cycle was repeated four times, one cycle to measure the temperature of the product in the center and at the edge vials and three cycles for the sublimated mass. Controlled nucleation was not used in the experiments, which means that ice structure formation was not uniform, which could lead to variations in product resistance in different runs. For protocol P1 after 11 h and for protocol P2 after 3 h the vials were removed from the dryer and weighed to  $\pm 0.01$  g accuracy using the Kern KB 650-2N balance. This was used to determine the average sublimated mass. Since three cycles were performed for the mass loss, this allowed the average drying behavior to be evaluated and helped to mitigate the effects of variability in product resistance. Based on the described procedure, the confidence interval for the obtained mean values of the measured temperatures and mass losses was calculated using Student's  $t$  distribution.

### 3. Computational model- multilevel model

In this paper, which presents a coupled numerical model for transport phenomena inside of freeze dryer and drying kinetics of the product in the vial, the basic idea is the following. The drying kinetics of a product inside each vial is simulated using a special 1D model (see Fig. 1) in which the pressure drop  $\Delta p$  experienced by the water vapor as it travels through the headspace of the vial is considered as an empirical correlation from the work of Kamenik et al. [18]. The reason for this is that the numerical grids required to adequately describe the flow pattern through the numerous vial headspace openings (the number of vials can range from a few hundred to a few thousand) would be extremely large, resulting in high computational costs and long simulation runs. In the work of Kamenik et al. [18], which studied a pressure drop within a single vial, one half of the vial was simulated, resulting in a grid of 282,000 elements for the CFD calculations. If the headspace above the product in each of the vials were modeled, this would yield numerical grids in the range of several million elements. The local drying kinetics of each vial depend on the local pressure value, which affects heat and mass transfer. The heat transfer from the heated shelf to the vial depends on the pressure value. The higher the local pressure, the higher the local heat transfer to the vial. The local pressure is also needed as a boundary condition for the 1D model that describes the drying kinetics of a product in the vial. There is a clear need to obtain the local flow conditions for the vials to evaluate the mutual influence of all vials and local pressure variations in the drying chamber. This is achieved by a proposed coupled numerical solution of heat and mass transfer within the product, which uses a 1D model describing the drying kinetics of a product inside the vial and the 3D flow in the drying chamber, and provides local pressure values for each vial calculated using computational fluid dynamics. In this work, a multilevel model is proposed using the TCP server, which connects the external standalone 1D program written in Fortran programming language with the commercial ANSYS Fluent code.

### 3.1. 3D CFD drying chamber model

The simulations of the flow through the drying chamber were performed using the ANSYS Fluent code [27]. The following governing equations describe the basic physical laws of fluid flow. The equation for the conservation of mass (continuity equation) is written as:

$$\frac{\partial \rho}{\partial t} + \nabla \cdot (\rho \vec{u}) = 0. \quad (1)$$

The local mass fraction of each species considered is predicted from the solution of the convection–diffusion equation. This conservation equation is written in the following form

$$\frac{\partial(\rho Y_j)}{\partial t} + \nabla \cdot (\rho \vec{u} Y_j) + \nabla \cdot \vec{J}_j = 0, \quad (2)$$

where and ( $\vec{J}_j$ ) is the diffusion flux of species  $j$ . The balance of the momentum is described by:

$$\frac{\partial(\rho \vec{u})}{\partial t} + \nabla \cdot (\rho \vec{u} \vec{u}) = -\nabla p + \nabla \cdot (\tau) + \rho \vec{g}. \quad (3)$$

The ANSYS Fluent code, which was used in the present work, solves the energy equation in the following form:

$$\frac{\partial(\rho E)}{\partial t} + \nabla \cdot (\vec{u}(\rho E + p)) = \nabla \cdot \left( k \nabla T - \sum_j h_j \vec{J}_j + (\tau_{eff} \cdot \vec{u}) \right), \quad (4)$$

where  $k$  is the thermal conductivity. The first term on the right-hand side of the equation represents energy transfer by conduction, the second term represents species diffusion, and the third term represents viscous dissipation. During the typical freeze-drying cycle, chamber pressures are extremely low (typically between 1 and 100 Pa). At this range, the Knudsen number increases above 0.01 and additional model modifications are needed [28]. We use the available Maxwell model to model the velocity slip and temperature jump on the walls, more in depth description of the model can be found in work of Kamenik et al. [18].

To calculate the density of a multicomponent compressible gas, an ideal gas model was used, which calculates the density using the following equation

$$\rho = \frac{p_{op} + p}{RT \sum_i \frac{Y_i}{M_{w,i}}}, \quad (5)$$

where  $p$  is the local relative (gauge) pressure predicted by ANSYS FLUENT and  $p_{op}$  is the operating pressure,  $Y_i$  is the mass fraction of the  $i$ th species and  $M_{w,i}$  is the molecular weight of the  $i$ th species.

#### 3.1.1. Fluid material properties

The following material properties were used for the calculation. For water vapor, the following values are used: Molar mass 18.015 kg/kmol, characteristic length  $\sigma = 2.605$  Å, energy parameter  $\epsilon/k_b = 572.5$  K, energy accommodation coefficient  $\alpha_c = 0.48$ , tangential accommodation coefficient  $\alpha_t = 0.91$  and specific heat  $c_{p,v} = 1859$  J/(kg K). For inert gas (nitrogen) the following values are used: Molar mass 28.0134 kg/kmol, characteristic length  $\sigma = 3.798$  Å, energy parameter  $\epsilon/k_b = 71$  K, energy accommodation coefficient  $\alpha_c = 0.45$ , tangential accommodation coefficient  $\alpha_t = 0.91$  and specific heat  $c_{p,v} = 1006$  J/(kg K). For viscosity, in both cases, the power relation  $\mu = \mu_{ref} (T/T_{ref})^n$  (power law) is used with the values for water  $\mu_0 = 8.9e-06$  Pa s,  $T_{ref} = 273$  K in  $n = 1$  [20], and for nitrogen  $\mu_0 = 1.66e-05$  Pa s,  $T_{ref} = 273$  K in  $n = 0.74$  [20]. A temperature-dependent thermal conductivity was prescribed, the values of which were obtained from the website NIST (National Institute of Standards and Technology, U. S. Department of Commerce) [29]. Thermal conductivity of the nitrogen and water vapor was prescribed as a linear function. For the nitrogen the thermal conductivity of 0.0204 W/(m K) at -50 °C and 0.0254 W/(m K) at +20 °C was used and for the water vapor the thermal conductivity of 0.015 W/(m K) at -50 °C and 0.017 W/(m K) at +20 °C was used.

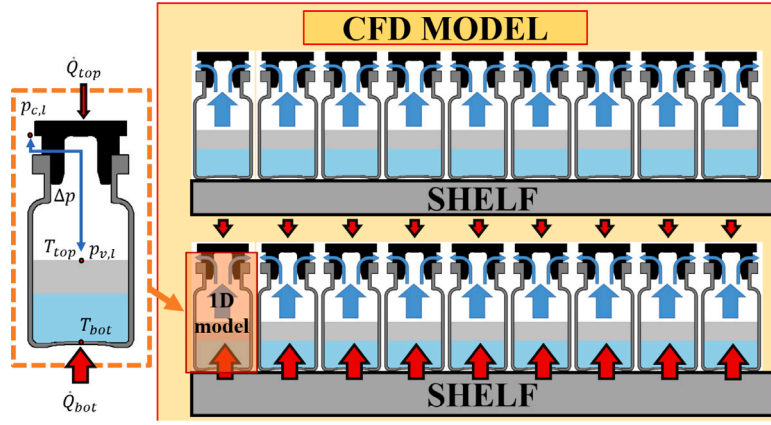


Fig. 1. Schematics of a coupled CFD-1D model for simulating drying kinetics of the product in all the vials in freeze dryer.

### 3.1.2. Numerical methods

The pressure-based segregated algorithm SIMPLE [27] was used for the calculations. Since the gas consists of two components ( $H_2O$ -vapor and  $N_2$ ), the species transport model was used. The following laws were used to calculate the mixture properties. For the specific heat: the mixing law, for the thermal conductivity and the viscosity of the mixture: the ideal gas mixture law, and for the calculation of the mass diffusivity: the kinetic theory. For the pressure discretization, PRESTO! (PREssure STaggering Option) was used, with a second order upwind scheme for density, momentum, species and energy.

### 3.2. Vial drying kinetics model

For the drying kinetics of the product inside the vial, the numerical model by Ravnik et al. [3] was used. The governing equations for the heat and mass transfer phenomena apply to the volume of the vial occupied by the frozen solution, in our case a mannitol-water mixture. The frozen region is considered as a homogeneous mixture with spatially independent material properties and the gas phase is modeled as a binary ideal gas mixture in thermal equilibrium with the porous cake. At the sublimation front, the equilibrium between the water vapor pressure and the solid ice is assumed. In Fig. 2, the heat and mass flows in the vial and the labels used are shown. In the Region 1 (cake) the heat is transferred due to vapor and inert gas convective fluxes (which implicitly include the effects of porosity in the  $N_i$  and  $N_v$  term, more details in the paper by Ravnik et al. [3]) as well as due to heat conduction, with additional heat sink due to desorption of water from the porous part of the drying substance. The conservation of energy for the Region 1 (cake) therefore reads as

$$\underbrace{\rho_1 c_{p,1} \frac{\partial T}{\partial t}}_{\text{accumulation}} + \underbrace{\vec{\nabla} \cdot ((\vec{N}_v + \vec{N}_i) c_{p,g} T)}_{\text{convection}} = \underbrace{\lambda_1 \nabla^2 T}_{\text{conduction}} + \underbrace{\Delta H_v \rho_{1,p} \frac{\partial C}{\partial t}}_{\text{desorption}} \quad (6)$$

where  $c_{p,g}$  is the specific heat for the mixture of water vapor and inert gas in Region 1 (cake),  $\lambda_1$  is thermal conductivity for a mixture of porous cake, water vapor and inert gas,  $c_{p,1}$  is the effective specific heat for a mixture of porous cake, water vapor and inert gas. In the Region 2 (frozen solution) the heat transfer mechanism is heat conduction, resulting in the following equation for the conservation of energy:

$$\underbrace{\rho_2 c_{p,2} \frac{\partial T}{\partial t}}_{\text{accumulation}} = \underbrace{\lambda_2 \nabla^2 T}_{\text{conduction}} \quad (7)$$

At the sublimation front, where the frozen and porous part of the domain are in contact, the ice undergoes the phase change, consuming the sublimation enthalpy for this process. At the sublimation front, the frozen region and the porous region have equal temperatures, however, due to different heat conductivities, moving front phenomena

and sublimation process, the heat fluxes in both parts of the domain are connected through the following interface condition:

$$\lambda_2 \left. \frac{\partial T}{\partial n} \right|_2 + \underbrace{v_n \rho_2 c_{p,2} T}_{\text{interface term}} = \lambda_1 \left. \frac{\partial T}{\partial n} \right|_1 + \underbrace{v_n \rho_1 c_{p,1} T}_{\text{interface term}} - \underbrace{\Delta H_s N_{v,n}}_{\text{sublimation}} - \underbrace{N_{v,n} c_{p,g} T|_1}_{\text{convection}} \quad (8)$$

where the condition  $\vec{N}_i = 0$  for the inert gas was considered. Conservation of mass needs to be computed only in Region 1 (cake), for both water vapor and inert gas, which are treated as ideal gases. Water vapor mass conservation reads as

$$\underbrace{\epsilon \frac{M_v}{R} \frac{\partial}{\partial t} \left( \frac{p_v}{T} \right)}_{\text{accumulation}} + \underbrace{\vec{\nabla} \cdot \vec{N}_v}_{\text{convection}} = - \underbrace{\rho_{1,p} \frac{\partial C}{\partial t}}_{\text{desorption}} \quad (9)$$

and inert gas mass conservation is

$$\underbrace{\epsilon \frac{M_i}{R} \frac{\partial}{\partial t} \left( \frac{p_i}{T} \right)}_{\text{accumulation}} + \underbrace{\vec{\nabla} \cdot \vec{N}_i}_{\text{convection}} = 0. \quad (10)$$

The critical part for the performance of the lyophilization models is a correct modeling of water vapor and inert gas mass fluxes. The gradient theory of mass transfer is applied, leading to expressions

$$\vec{N}_v = - \frac{M_v}{RT} (k_1 \vec{\nabla} p_v + k_2 p_v (\vec{\nabla} p_v + \vec{\nabla} p_i)) \quad (11)$$

$$\vec{N}_i = - \frac{M_i}{RT} (k_3 \vec{\nabla} p_i + k_4 p_i (\vec{\nabla} p_v + \vec{\nabla} p_i)) \quad (12)$$

where  $k_1$ ,  $k_2$ ,  $k_3$  and  $k_4$  are diffusivities. More details about the implementation of the model can be found in work of Ravnik et al. [30].

Initially, the volume consists only of ice (frozen product) and as drying progresses, a porous cake is formed. To avoid numerical difficulties associated with the moving grid, an initial thickness of the dried region of 2% of the total cake height is prescribed [31,32]. The governing equations of heat and mass conservation for the one-dimensional approximation of the vial were discretized using the finite difference method. The central differencing scheme was used for the spatial derivatives and the backward Euler scheme for the temporal derivatives. Numerical simulations of the freeze-drying of the mannitol solution were performed with 50 grid points uniformly distributed between the solid and porous parts of the domain, and with a time step of 1 s, as established in a previous work [3]. The initial height of the cake was  $h_{fill} = 6.706$  mm. The start of the one-dimensional model was  $z_{inf,start} = 0.98$  L. At the bottom, when the sublimation interface reached 2% of the total height, the simulation of the primary drying phase was continued using a simple linear algebraic model [31] with extrapolated drying kinetics by using the last one-dimensional calculated drying rate to calculate the removal of the bottom 2% of the ice.

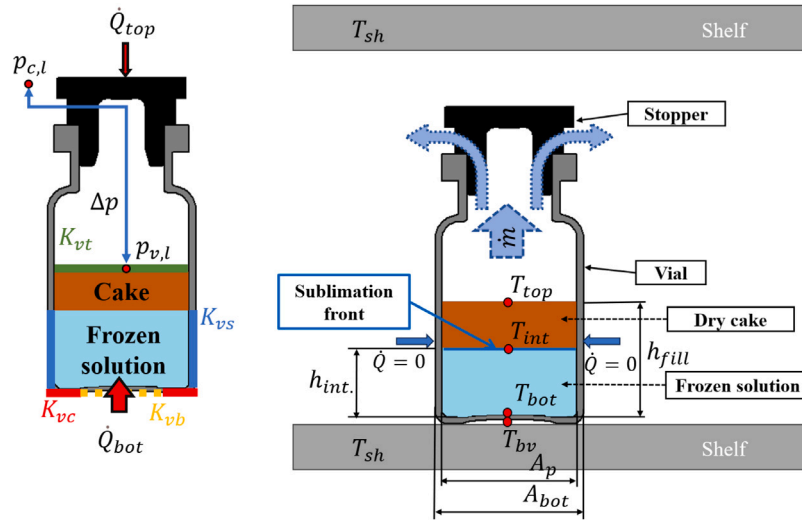


Fig. 2. Heat and mass flows in the vial and the labels used.

### 3.2.1. Boundary conditions

For 1D model, pressure boundary condition is needed on the cake-air interface. The water vapor partial pressure is set as

$$p_{v,l} = p_{c,l} x_{v,l} + \Delta p_{s,l} \quad (13)$$

where  $p_{c,l}$  is the local chamber pressure above the vial and  $x_{v,l}$  is the local mole fraction of the water vapor. For the local pressure increase inside of the vial headspace  $\Delta p_{s,l}$ , correlation proposed by Pikal [2] for water vapor flow in the form of pressure resistance is used

$$\Delta p_{s,l} = \dot{m}_l R_s, \quad (14)$$

where  $\dot{m}_l$  [g/h] is the sublimate vapor mass flow,  $\Delta p_{s,l}$  [Pa] is the pressure drop in vial headspace, and  $R_s$  [(Pa h)/g] is the stopper resistance describing the predominantly viscous flow with a contribution from the Knudsen flow. Resistance, that depends on the chamber pressure [2] is calculated from the following expression

$$R_s^{-1} = a + b\bar{p}, \quad (15)$$

where  $\bar{p}$  is the mean pressure across the barrier (through the closure)  $\bar{p} = (p_{c,l} + p_{v,l})/2$  and  $a$  and  $b$  are model constants. Since the 10R vial has the same neck width and the rubber stopper geometry as the 6R vial, the values for the  $a = 0.0658$  g/(Pa h)  $b = 0.015$  g/(Pa<sup>2</sup> h) were used, taken from the work [18].

The Ravnik model [3] in its basic form requires a prescribed coefficient  $K_v$ , but in this case, we want this coefficient to update according to the local pressure value above the vial. The heat flow rate to the bottom of the vial  $\dot{Q}_{bot}$  (applied to the bottom of the frozen domain) is proportional to the overall heat transfer coefficient  $K_v$  and the temperature difference between the shelf temperature  $T_{sh}$  and the temperature at the bottom of the vial  $T_{bot}$ :

$$\dot{Q}_{bot} = K_v A_{bot} (T_{sh} - T_{bot}), \quad (16)$$

where the heat transfer coefficient is calculated based on the local pressure (derived from the total pressure above the vial), which is computed by the CFD model for each time step. With thermal radiation, part of the heat is supplied via the upper surface (applied to the top of the cake). The heat flow to the cake-air interface is calculated as

$$\dot{Q}_{top} = \sigma F_{12,t} A_{bot} (T_{sh}^4 - T_{top}^4), \quad (17)$$

where  $F_{12,t}$  is the view factor. The calculation of the heat transfer coefficient  $K_v$  is based on the heat transfer model presented in the following subsection.

### 3.2.2. Calculation of pressure dependent heat transfer coefficient

In this paper, the constant vial heat transfer coefficient is used. The calculation of the heat transfer coefficient is based on the heat transfer model presented in work of Ramšak et al. [33]. The heat transfer coefficient of the vial consists of multiple heat inputs through different surfaces of the vial. Heat is added by conduction (through the contact surface between the vial and the shelf), by thermal radiation from the heated shelves, and by conduction through the gas inside the drying chamber. The effect of fluid motion inside the drying chamber (convection) can be neglected due to the very low system pressure. On the other hand, the effect of additional heat radiation from the walls of the drying chamber on the vials located at the edge of the shelf is present [34,35]. Due to the curvature at the bottom of the vial, only part of the bottom surface of the vial is in direct contact with the shelf and for the remaining surface there is a gap between the bottom surface of the vial and the shelf.

On the other hand, the vial packing density additionally affects the heat transfer rate to a vial, as reported in the works of Gieseler & Lee [36], Hibler et al. [37], and more recently Ehlers et al. [38], and Matejčíková and Rajniak [39]. This is typically accounted for by introducing the packing factor (PF) when considering the heat transfer from the shelf. For the surface of the vial that is in direct contact with the shelf, the heat transfer coefficient  $K_{vc}$  is

$$K_{vc} = K_{vc,exp} \frac{A_{bot}}{A_{cont}} \frac{PF_C}{PF} \quad (18)$$

where  $A_{cont}$  is the contact area and  $K_{vc,exp}$  is the heat transfer coefficient due to direct contact (experimentally determined to represent in this case only the conductive heat transfer through the contact area, taken from the work of Scutella et al. [35]). It is defined over the entire bottom surface of the vial to ensure uniform scaling, but does not include contributions from other mechanisms such as radiation or conduction through the gas layer. In the present work, the value of  $A_{cont}$  is taken from the literature [33] and corresponds to 15.7% of the bottom area of the vial. The  $PF_C$  is the packing factor for the central vial, and  $PF$  is the packing factor for the local vial, which depends on the position of the vial. The spatial variation is shown in Fig. 3(b).

In the gap between the shelf and the bottom of the vial, heat is transferred by two mechanisms. Part of the heat is transferred by thermal radiation between the two surfaces [2] and the second mechanism is conduction through gas

$$K_{vb} = \sigma F_{12,b} (T_{sh,pd} + T_{bv}) (T_{sh,pd}^2 + T_{bv}^2) + \frac{C_2 p_c}{1 + \frac{l_b}{\lambda_{amb}} C_2 p_c} \quad (19)$$

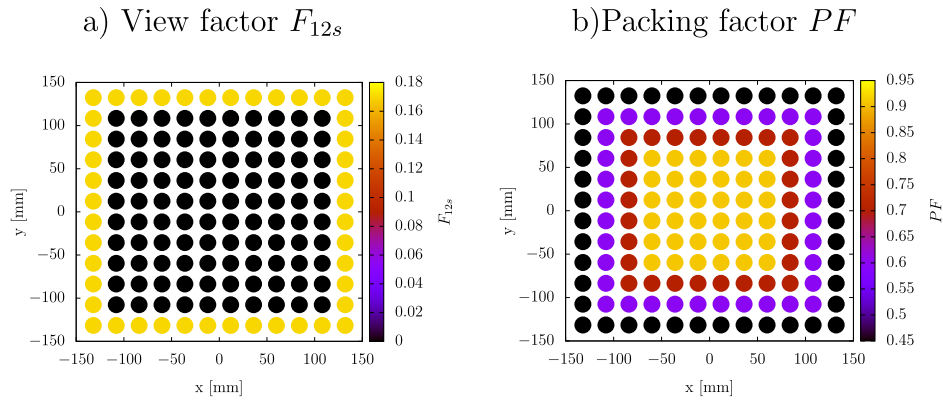


Fig. 3. View factors and packing factors depending on the location of the vial on the shelf. The same applies for both shelves [36].

with

$$C_2 = A_0 \left( \frac{\alpha_c}{2 - \alpha_c} \right) \left[ \frac{273.15}{T_{gas}} \right]^{0.5}, \quad (20)$$

$$F_{12,b} = \frac{1}{\left[ 1 + \left( \frac{1}{\epsilon_{glass}} - 1 \right) + \left( \frac{1}{\epsilon_{shelf}} - 1 \right) \right]} = 0.17, \quad (21)$$

where  $p_c$  is the pressure inside the chamber,  $T_{vb} = 0.75T_{sh,pd} + 0.25T_{sh,f}$  is the temperature of the vial at the bottom,  $T_{gas} = T_{sh,pd}$  is the gas temperature approximated as the shelf temperature,  $\sigma$  is the Stefan-Boltzmann constant,  $\lambda_{amb}$  is the free molecular thermal conductivity of the water vapor,  $F_{12,b}$  is the effective view factor for the bottom, the parameter  $C_2$  accounts for the free molecular flow heat transfer coefficient  $A_0$ ,  $\alpha_c$  is the thermal accommodation coefficient, and  $l_b$  is the integral conduction length at the bottom of the vial ( $l_b = 1/3 \cdot h_{gap,b}$ ). The first term describes the thermal radiation and the second term the conduction through the gas. The view factor  $F_{12,b}$  is calculated with the values  $\epsilon_{glass} = 0.78$  and  $\epsilon_{shelf} = 0.18$ . Due to the temperature difference between the side wall of the vial and the shelves, heat is transferred to the side of the vial by conduction through the gas in addition to thermal radiation, and then transfer by conduction through the glass wall, i.e.

$$K_{vs} = \sigma F_{12,s} (T_{sh,pd} + T_{vial}) (T_{sh,pd}^2 + T_{vial}^2) + \frac{1}{\frac{1}{C_2 p_c} + \frac{l_{ss}}{\lambda_{amb}} + \frac{\delta_{glass}}{\lambda_{glass}}} \quad (22)$$

where  $F_{12,s}$  is the effective view factor for the side wall,  $\delta_{glass}$  is the wall thickness of the vial, and  $l_{ss} = h_{fill}/3$  is the integral conduction length at the side of the vial. The vials on the side (exposed to the chamber walls) receive part of the heat through thermal radiation from the surrounding walls, while the central vials are protected from this. Therefore, a spatially dependent distribution is used for the view factor  $F_{12,s}$ , specifically 0.18 for the side vials and 0 for the central vials (the same for both shelves), as shown in Fig. 3a. (As the freeze dryer is located in an air-conditioned room and the front door on the side facing the chamber is fitted with a low-emissivity radiation shield and thermal insulation, the radiation and convection effects of the front door were considered negligible). The overall heat transfer coefficient  $K_v$ , defined to the outer cross section of the vial, which takes into account the heat transfer through the bottom and the side wall of the vial is calculated as

$$K_v = (K_{vs} A_{side} + K_{vb} (A_{bot} - A_{cont.}) + K_{vc} A_{cont.}) / A_{bot} \quad (23)$$

where  $A_{side} = \pi d_p h_{side}$  is the area of the side of the vial, which is decreasing as the drying is progressing ( $h_{side} = h_{int.} + h_{gap,b}$ , dimension shown on Fig. 2). The values of the model parameters used are summarized in Table 2.

Table 2

Values of model parameters.

Variable	Value
$\lambda_{glass}$	1.1 W/(mK)
$\lambda_{ice}$	2.54 W/(mK)
$\lambda_{amb}$	0.025 W/(mK)
$\sigma$	$5.67 \cdot 10^{-8}$ W/(m <sup>2</sup> K <sup>4</sup> )
$\Delta h_{sub}$	$2840.2 \cdot 10^3$ J/kg
$\rho_{ice}$	920.4 kg/m <sup>3</sup>
$K_{vc}$	3.67 W/(m <sup>2</sup> K)
$F_{12,s}$	0.0
$F_{12,t}$	0.17
$\alpha_c$	0.46
$A_0$	1.99 W/(m <sup>2</sup> KPa)
$\delta_{glass}$	0.001 m
$l_b$	$2.33 \cdot 10^{-4}$ m
$d_v$	0.024 m
$d_p$	0.022 m
$h_{gap,b}$	0.0007 m
$T_{freeze}$	-35 °C

### 3.3. Coupling models with TCP server

In this case, two separate programs simulate different aspects of the transport phenomena during freeze-drying: the drying kinetics inside the vial (modeled in Fortran with the finite difference method) and the flow field through the drying chamber (modeled with CFD ANSYS Fluent). These programs work independently of each other and exchange key values to ensure consistency. The CFD code requires the boundary conditions from the Fortran program (gas temperature and sublimated mass flow rate), while the Fortran program requires the local pressure values from the CFD simulation. Data is exchanged via a TCP-based network socket, with both programs connecting to a central server (Fig. 4). At the beginning, the Fortran program sends the temperature of the shelf to the CFD solver, which calculates the flow field. At each time step, the CFD program calculates area-weighted average pressures at the vial inlets and transmits them to the Fortran program, which updates the drying kinetics and provides new gas temperatures and mass flow rates. This iterative exchange continues until the simulation has reached the specified time limit.

### 3.4. Geometrical model and boundary conditions

The final model includes the geometry of the drying chamber and part of the geometry of the rubber stopper. As 10R vials were used in the experiment, the gap height is 19.5 mm. For the performed computations the top surface of the stopper also modeled, leading to a more realistic topology of the space between the row of vials and the shelf above them. At each local inlet (shown in red at the bottom of Fig. 4), the gas mass flow rate and the temperature are set,

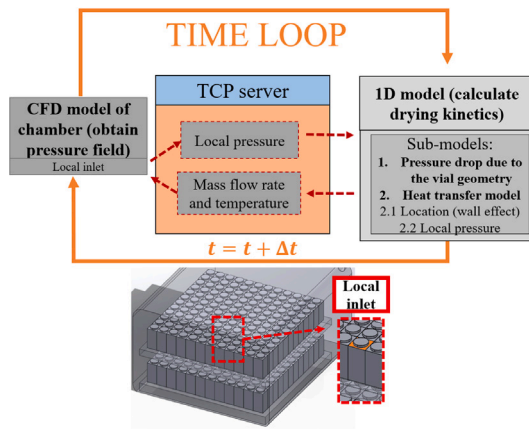


Fig. 4. The multilevel coupling scheme and the exchange of data between the codes.

provided by an external Fortran code while it computes a new gas mass flow rate and temperature for each time step. A mass flow rate of 1.6 g/h was specified for nitrogen at the surface through which the nitrogen is supplied. At the outlet, located inside the duct leading to the condenser, a static pressure of 0 Pa was specified, which, together with the specification of an operating pressure within the computational domain, ensures the correct system pressure conditions (e.g. if the operating pressure is 6 Pa, an absolute pressure of 6 Pa is prescribed). The time-dependent temperature of the shelf was specified for the shelf surfaces. This was used to model the influence of the heated shelves on the gas properties inside the drying chamber. In this way, we model the mixing of the cold water vapor produced during sublimation with the warmer gas inside the chamber. For the outer walls, which are in contact with the environment, a temperature of 10 °C was specified. For the side walls of the vials (rim vials), the adiabatic boundary condition was prescribed (the heat radiation contribution to the sides of the vials is taken into account in the 1D vial model, with Eq. (22)). The heat conducted into the vial through the shelf is modeled separately by the external 1D model, as described in Section 3.2.1.

Two sets of calculations were performed at different shelf temperatures. For first protocol (P1), the prescribed operating pressure was 22 Pa with the shelf temperature of −20 °C and for the second protocol (P2), the shelf temperature was +10 °C.

Three computational grid densities were considered and validated with steady-state simulations. For the operating pressure 8 Pa was used, +10 °C for the shelf temperature and sublimation mass flow from each vial 0.504 g/h. Lower pressure value compared to the experiment (in experiment, chamber pressure was 22 Pa) was used, since later we also performed parametric study at lower pressures. The coarse grid had 522,000 elements, medium 1,313,000 and fine 1,972,000 elements. Based on the obtained results, the Richardson extrapolation was used to compare the pressure values above the vial located at the center of the bottom shelf. The grid refinement ratio was 1.32 for fine and medium mesh, and 1.38 for medium and coarse mesh, resulting to GCI (Grid convergence index) of 0.006% between the fine and medium mesh and 0.009% between the medium and coarse mesh. As there are almost negligible differences between all the considered meshes, for the final calculations the coarse grid was chosen. A time-step size of 1 s was chosen for the ramp-up part and a larger time-step size of 100.0 after first 100 s. In the CFD the convergence criterion was set at RMS of  $10^{-6}$  for continuity, momentum and energy equations. The 1D model was coupled to the CFD model through the TCP server, as a solver for drying kinetics for each separate vial based on the pressure results above each separate vial from the CFD model.

## 4. Results and discussion

### 4.1. Validation of the multilevel model

Fig. 5 shows the time-dependent temperature at the bottom of the central and the edge vial at shelf temperature of −20 °C. Based on the experimental results, we can see that the temperature at the bottom of the vial increases with increasing shelf temperature until the drying temperature in the quasi-steady state is reached. The same trend is observed in the numerical results, where the temperature is within the confidence interval of the measurements. The vial at the edge has about 15% shorter drying time compared to the central vial due to more heat being received from the surrounding walls by thermal radiation and also due to the fact that the edge vials have fewer neighboring vials and they can pump heat from a larger shelf area, which is accounted for by applying the packing factor. However, it is important that the mass flow rates are correct in addition to the correct drying temperature. From Fig. 6(b) and (c) we can see that both vial results fall within the confidence interval for the percent dry. However, the confidence intervals for the percent dry are quite wide, especially for the central vial. Fig. 6 shows the time-dependent temperature at the bottom of the central and edge vial at a shelf temperature of +10 °C. In this case, we can see that the trend is similar at higher shelf temperature, but the temperature increases more steeply and the drying times are shorter. The vial at the edge has about 20% shorter drying time compared to the central vial. As the temperature at the bottom of the vial rises, the numerical model initially overestimates the temperature. However, once the quasi-steady-state temperature is reached, the predictions align with experimental measurements. The percent dry values also fall within the confidence interval, though the interval width remains comparable to that observed at lower shelf temperatures. The broad confidence intervals are attributed to uncontrolled nucleation, which results in variations in pore size and, consequently, differences in permeability. This effect is more pronounced at lower shelf temperatures, where the extended drying cycles amplify these variations.

The higher temperatures observed at the bottom of the vial, which exceed the specified shelf temperature, are due to heat transfer by radiation from the surrounding walls. In our analysis, radiation is taken into account in a simplified way, with calculations based on the shelf temperature and the prescribed heat transfer coefficient ( $K_v$ ) for the vials.

### 4.2. Primary drying time

Fig. 7 shows the primary drying times for all vials on the bottom shelf at different shelf temperatures. As we can see, in both cases, the vials at the edge of the shelf dry the fastest, with the drying time increasing towards the center of the shelf. However, the vials in the middle are not the slowest, the vials with the slowest drying time are the edge vials in the fourth row (from the edge row inwards), which is due to the lower local pressure above the vial, resulting in less heat being applied to the vial (Fig. 8(a)). Fig. 8 shows the local pressure at the vial locations at two time instants, at a primary drying time of 11 h for the shelf temperature of −20 °C and 3 h for the shelf temperature of +10 °C. As can be seen in Fig. 8(a), the local pressure is highest at the front center of the bottom shelf and decreases towards the rear wall where the connecting duct is located. At higher shelf temperature, the maximum pressure across the vials at the bottom shelf is about 0.4 Pa, compared to 0.1 Pa at lower shelf temperature.

### 4.3. Flow conditions in the lyophilizer at the maximum mass flow of primary drying

After initial ramp up of the shelf temperature, the drying proceeds under maximum sublimation mass transfer rates, as the porous cake in the vial is just starting to form and its influence on mass transfer is

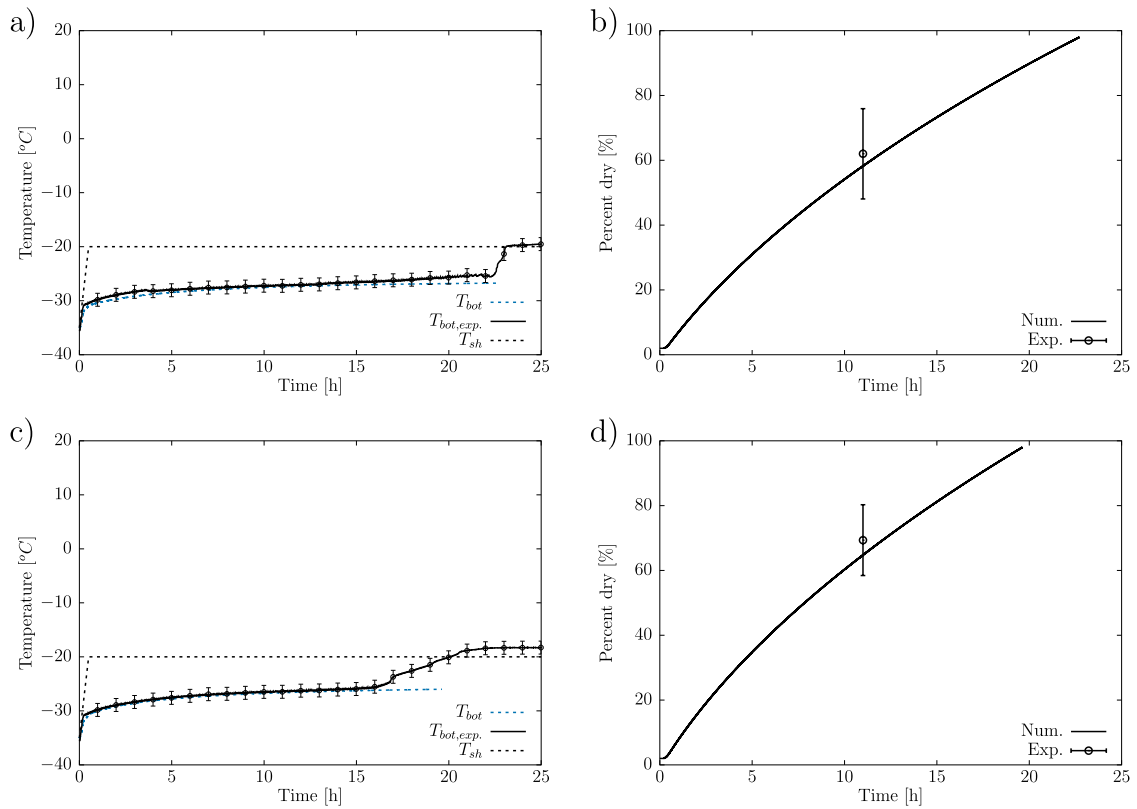


Fig. 5. Average temperature at the bottom of vial for shelf temperature of  $-20\text{ }^{\circ}\text{C}$  located (a) in the center of the shelf and (c) on the edge, and percent dry for the (b) central vial and (d) edge vial.

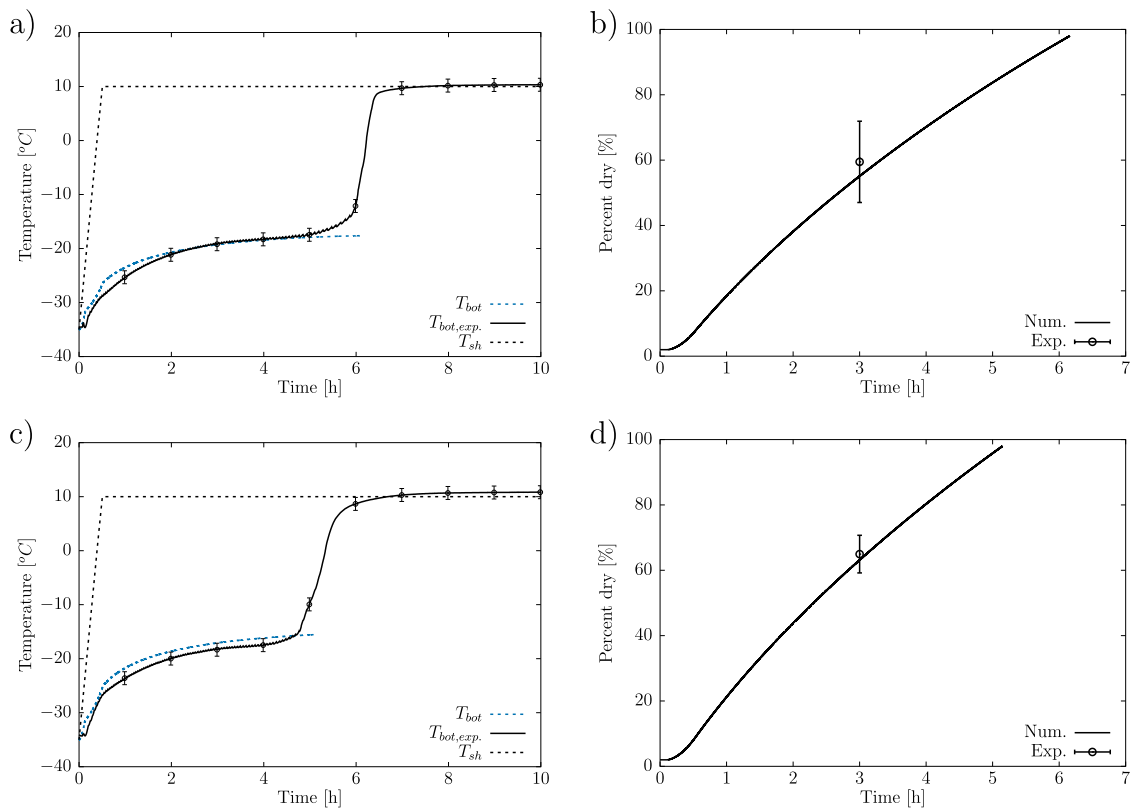


Fig. 6. Average temperature at the bottom of vial for shelf temperature of  $+10\text{ }^{\circ}\text{C}$  located (a) in the center of the shelf and (c) on the edge, and percent dry for the (b) central vial and (d) edge vial.

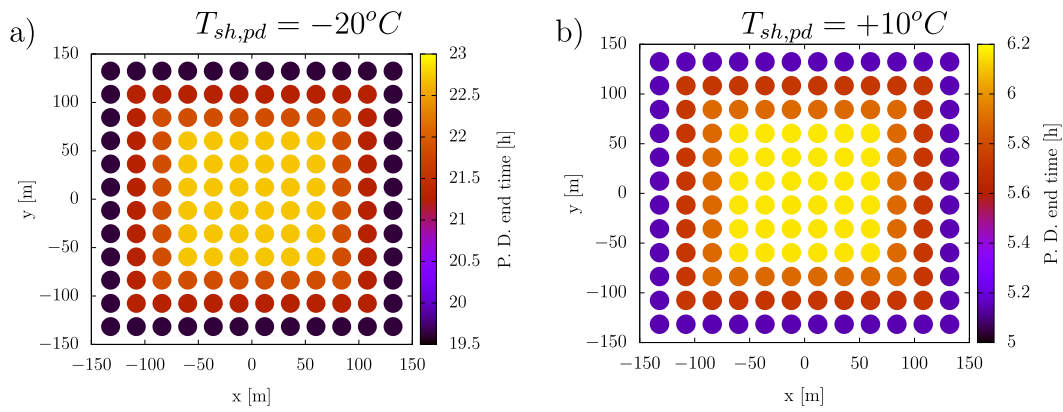


Fig. 7. Primary drying times for each vial located on the bottom shelf (a) for shelf temperature of  $-20^{\circ}\text{C}$  and (b) for shelf temperature of  $+10^{\circ}\text{C}$ .

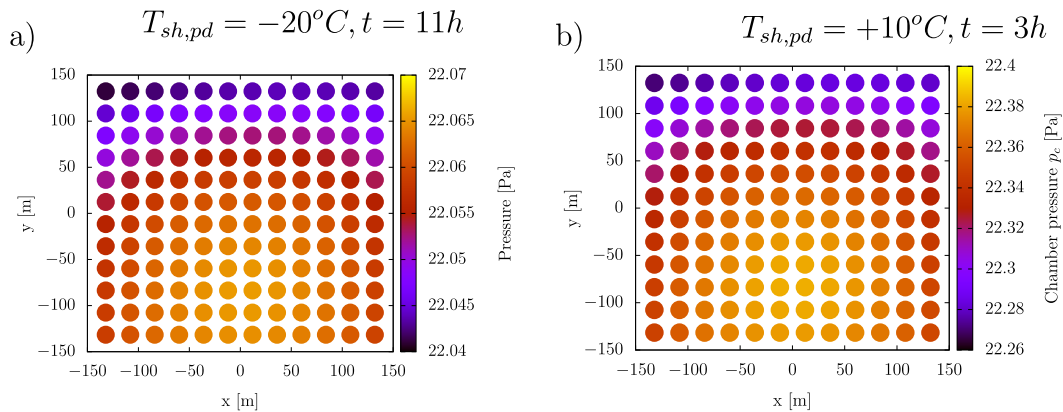


Fig. 8. Pressure values across the 10R vials at the bottom shelf at different shelf temperatures. (a) Results at a shelf temperature of  $-20^{\circ}\text{C}$  after 11 h of drying. (b) Results at a shelf temperature of  $10^{\circ}\text{C}$  after 3 h of drying.

therefore the lowest. In Fig. 9 we see the water vapor flow through the system at both tested shelf temperatures. As we can see, the pattern is the same in both cases (there are no significantly different flow structures) with the water vapor flowing relatively slowly through the volume of the drying chamber and then accelerating significantly as it enters the connecting duct. Also, at a higher shelf temperature the velocities are a much higher due to higher sublimation rates. The maximum drying rates occur approximately after 0.5 h of primary drying, leading to a maximum impact of the pressure increase in the drying chamber on the drying kinetics in the vials. As can be seen in Fig. 10, the system pressure increases above the vials located on the bottom shelf. At a shelf temperature of  $-20^{\circ}\text{C}$ , the pressure above the central vials on the bottom shelf increases by about 0.1 Pa (absolute pressure 22.07 Pa), while at a higher shelf temperature, where the sublimation mass flow rate is higher, the pressure increases by about 0.5 Pa (absolute pressure 22.4 Pa). Above the top shelf, however, we see that there is no local increase in pressure as the water vapor has more volume to expand into.

If we look at the velocity fields (Fig. 11), we see that the water vapor velocities in the system are relatively low at the lower temperature of the shelf because the sublimation rate is low, and we notice that the water vapor accelerates in the area to the left above the upper shelf. The increase in velocity in this region is due to the fact that all the water vapor generated in the system is directed into the connecting duct to the condenser. The same behavior, but even more pronounced, is observed at a higher temperature of the shelf, where we see that the velocities are much higher (higher sublimation rate) and the increase in velocity towards the connecting duct is also more pronounced. As observed on Fig. 12, at a higher shelf temperature, the temperatures in the system are relatively uniform, because the cold water vapor that

flows into the gap between the shelf and the top of the vials heats up to a higher temperature, while at a lower shelf temperature we see that the temperature in the gap is lower. The cold water vapor is only heated there to the temperature of the shelf ( $T_{sh,pd} = -20^{\circ}\text{C}$ ). When it then comes into contact with the walls of the chamber, it heats up even more, as the temperature difference between the shelf and the surrounding walls is higher.

#### 4.4. Influence of temperature and pressure increase above the shelf on 10R and 15R vials

In addition to the simulations carried out for 22 Pa, a numerical simulation was also carried out at a chamber pressure of 6 Pa, with the initial product temperature set to  $-42^{\circ}\text{C}$ . This setting, which ensures gentle freeze-drying and is therefore frequently chosen in pharmaceutical practice, represents a case in which the influence of the local pressure increase on the heat transfer to the vials as well as on the mass transfer rate is greatest. To investigate the effects of the local pressure increase, the primary drying times for a chamber pressure of 6 Pa, the temperature at the bottom of the product (minimum and maximum temperatures at the bottom of the product) and the temperature of the product at the end of drying (at which time these are at their highest) are shown below. The results are compared with uncoupled results using a constant pressure boundary condition for  $p_c$  (set as chamber pressure, 6 or 22 Pa) when calculating the 1D heat and mass transfer within a vial. Figs. 13 and 14 illustrates the local pressure fluctuations above the vials and in the headspace of the vials for 10R and 15R vials at a chamber pressure of 22 Pa. As can be observed, the pressure increase above the 10R vials at a low shelf temperature of  $-20^{\circ}\text{C}$  is minimal, about 0.1 Pa. When the shelf temperature is

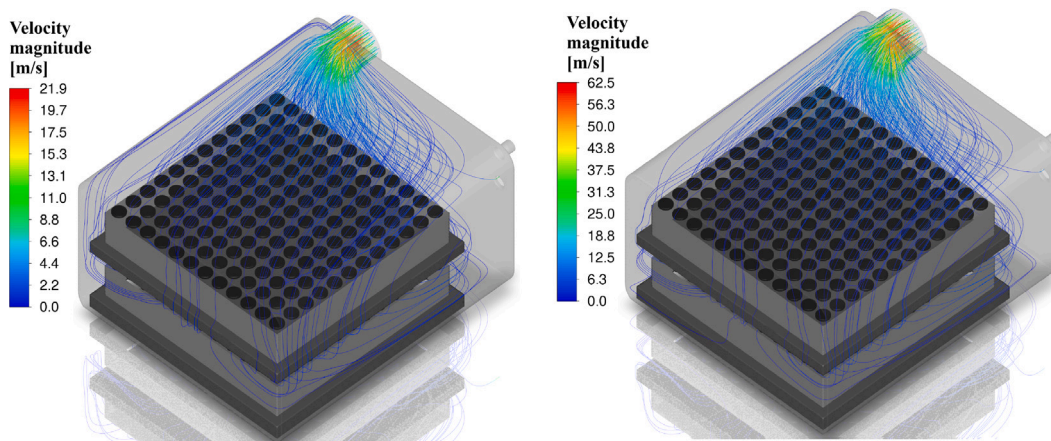


Fig. 9. Streamlines in the entire system (a) for shelf temperature of  $-20\text{ }^{\circ}\text{C}$  and (b) for shelf temperature of  $+10\text{ }^{\circ}\text{C}$ .

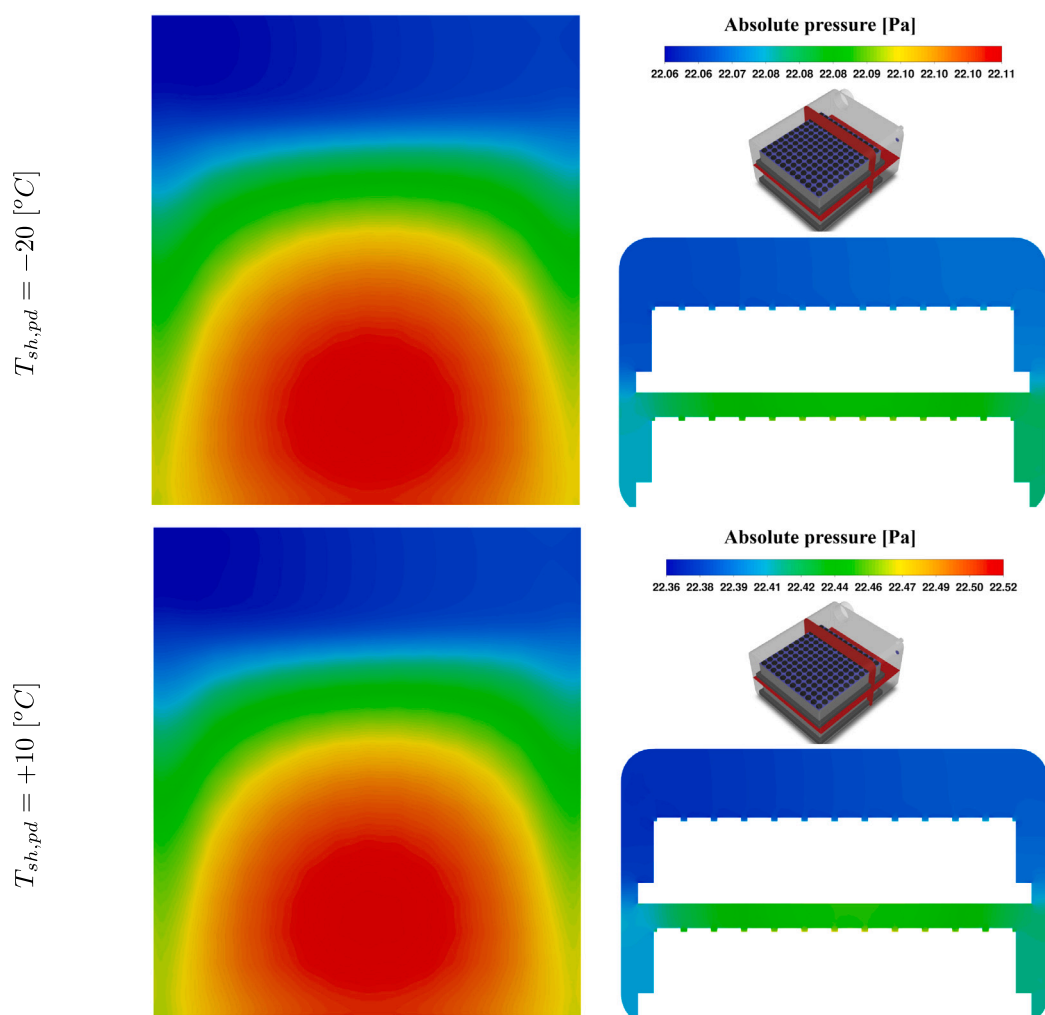


Fig. 10. Pressure fields along cross-sectional planes after 0.5 h of primary drying, at shelf temperatures  $T_{sh,pd} = -20$  and  $+10\text{ }^{\circ}\text{C}$  (separate legends for each shelf temperature).

increased to  $10\text{ }^{\circ}\text{C}$ , the pressure increase becomes more pronounced and reaches about  $0.5\text{ Pa}$ . However, the pressure in the headspace of the vial increases more, namely by about  $0.25\text{ Pa}$  at a shelf temperature of  $-20\text{ }^{\circ}\text{C}$  and by up to  $1\text{ Pa}$  at a shelf temperature of  $10\text{ }^{\circ}\text{C}$ . With the 15R vials, a much higher local pressure increase is observed above the vials. This is due to the smaller gap between the top of the rubber stoppers and the shelf above, which restricts the vapor flow and leads

to a greater increase in pressure. In contrast, the 10R vials have a larger gap so that the vapor can escape better and the pressure increase is lower. While the pressure difference between the top of the dried cake and the chamber pressure remains almost constant, the pressure increase in the headspace is much more pronounced at higher shelf temperatures. At a shelf temperature of  $10\text{ }^{\circ}\text{C}$ , the pressure in the headspace of the vial rises by about  $4\text{ Pa}$  before gradually decreasing

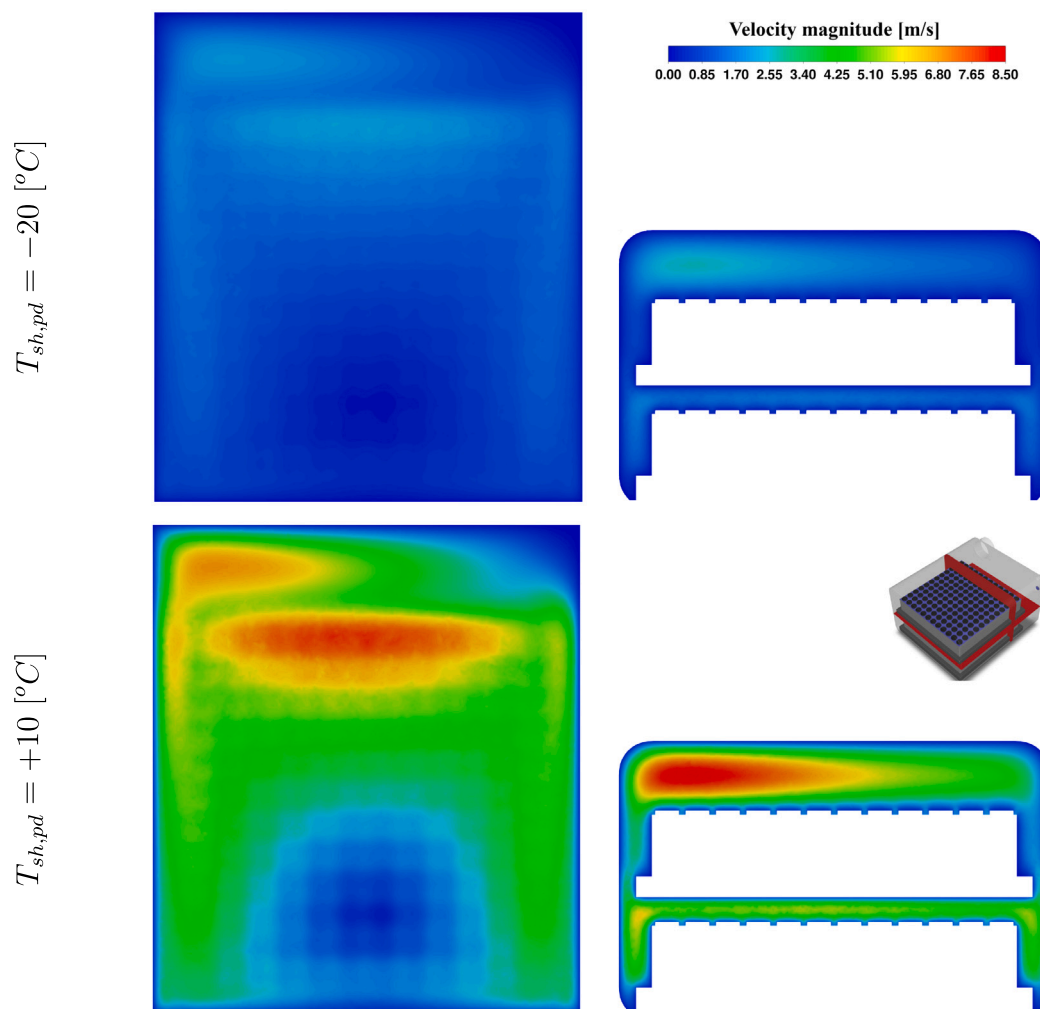


Fig. 11. Velocity fields along cross-sectional planes after 0.5 h of primary drying, at shelf temperatures  $T_{sh,pd} = -20$  and  $+10$  °C (unified legend for comparison).

as the mass flow rate decreases. A similar trend can be observed for the edge vials, although the effect is less pronounced compared to the central vials. Fig. 14 shows local pressure variations above and in the headspace of 10R and 15R vials at 6 Pa. Compared to 22 Pa, pressure increases more due to lower system pressure and higher sublimation flow. For 15R vials, the increase is even more pronounced due to the smaller gap between the rubber stopper and shelf above. At  $-20$  °C, pressure above central vials rises by 1 Pa, while at  $10$  °C it peaks at 4 Pa before gradually decreasing. Headspace pressure also rises, reaching nearly 6 Pa at the highest shelf temperature. Edge vials show similar trends but with a smaller effect. These results confirm that at lower chamber pressures, restricted vapor flow over 15R vials significantly increases local pressure and heat transfer. Figs. 16 and 15 show the bottom product temperature ( $T_{bot}$ ) for uncoupled and coupled results. In Fig. 15, differences are minimal at 22 Pa and  $-20$  °C for 10R vials. However, 15R vials show greater deviation, indicating headspace pressure drop and increased heat supply affects product temperature more when the gap above the stopper narrows. At  $10$  °C, higher sublimation mass flow amplifies differences for both vials, especially for 15R, as increased pressure enhances heat transfer and headspace pressure. At 6 Pa (Fig. 16), differences between coupled and uncoupled results are more pronounced. For 10R vials at lower shelf temperatures, deviations remain small and sometimes negligible. However, 15R vials show a significant temperature increase as heat supply and headspace pressure rise, indicating stronger pressure-induced heat transfer. Differences grow at higher shelf temperatures: for 10R, bottom temperature

is  $2$  °C higher in the coupled model, while for 15R, it is  $4$  °C higher, decreasing as drying ends due to decrease of local pressure (Fig. 14). This highlights the importance of coupled models, especially for aggressive drying cycles where high temperatures risk product collapse. Since product temperature affects collapse risk, a coupled model ensures more accurate thermal assessment, improving process control and product quality. Fig. 17 shows bottom vial temperatures at the end of primary drying. 10R vials are arranged in four levels, with edge vials drying at higher temperatures due to greater heat supply. The highest temperatures occur in edge vials, followed by the second and third rows, with the lowest in the center. Differences between uncoupled and coupled results are larger at lower pressure and  $+10$  °C shelf temperature. At lower pressures and higher shelf temperatures, increased local pressure and headspace pressure drop affect heat input more, especially in 15R vials. In the central region, 15R vials show greater temperature deviations than 10R. Headspace pressure drop also intensifies temperature fluctuations, emphasizing that pressure-related heat and mass transfer effects increase as the gap above the stopper narrows. Table 3 shows maximum, minimum, and average primary drying times with standard deviation for all vials and separately for the bottom and top shelves. Comparing maximum drying times from the coupled and uncoupled models (neglecting vial pressure increase), at  $-20$  °C and 22 Pa, the center 10R vial dries 0.22 h (1%) faster with coupling, while the 15R vial dries 0.24 h (1%) slower. At  $+10$  °C, drying time decreases by 0.16 h (2.5%) for 10R and 0.14 h (2.2%) for 15R. These results suggest that at lower shelf temperatures, pressure

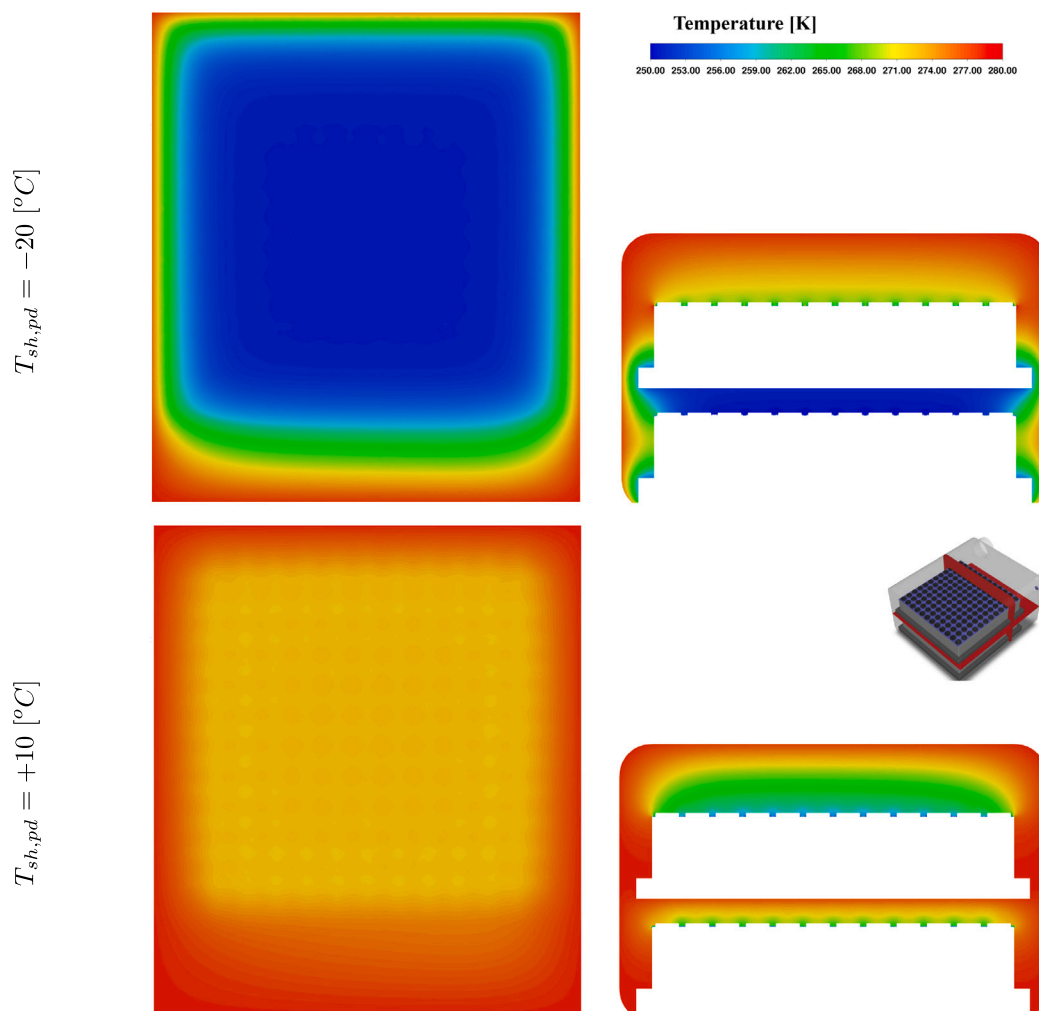


Fig. 12. Temperature fields along cross-sectional planes after 0.5 h of primary drying, at shelf temperatures  $T_{sh,prd} = -20$  and  $+10$  °C (unified legend for comparison).

buildup above 10R vials enhances heat transfer enough to counteract internal pressure effects, as sublimation is slower. In 15R vials, however, increased headspace pressure slows mass transfer. At higher shelf temperatures, faster drying occurs in both cases, as external pressure buildup compensates for internal pressure effects. At 22 Pa, drying times on both shelves are similar for 10R and 15R vials at  $-20$  °C, with no significant differences at  $+10$  °C. However, at 6 Pa, notable differences emerge. At  $-20$  °C, 15R vials on the bottom shelf dry in 24.33 h, compared to 23.7 h for 10R vials (3% longer), suggesting local pressure buildup slows mass transfer. At  $+10$  °C, differences increase; while 10R vials remain largely unaffected, 15R vials dry faster (8.72 h vs. 9.09 h for 10R, a 4% decrease), due to a smaller stopper-shelf gap increasing pressure and improving heat transfer. At 6 Pa and  $-20$  °C, coupling reduces drying time by 0.67 h (2.7%) for 10R vials but only 0.04 h (0.1%) for 15R vials. At  $+10$  °C, reductions are 0.66 h (6.7%) for 10R and 1.03 h (10.5%) for 15R. In all cases at 6 Pa, pressure buildup improves heat transfer, offsetting resistance effects. Standard deviation data show shelf uniformity improves at 6 Pa for 15R vials. At  $-20$  °C, bottom shelf deviation is 0.15 h (7%) lower than the top shelf. At  $+10$  °C, the difference grows to 0.3 h (30.9%). This suggests pressure buildup enhances drying uniformity on the bottom shelf. These results illustrate the importance of using a coupled model, especially when the gap between the rubber stopper and the shelf above is small and the chamber pressure is 6 Pa and below. Under such conditions, the interactions between pressure build-up, heat transfer and mass transfer influence the drying behavior considerably, so that a simplified uncoupled approach is not sufficient.

## 5. Conclusions

The conducted study demonstrates the improved effectiveness of the coupled multilevel computational model in predicting drying behavior in vial lyophilization. The findings highlight the impact of local pressure variations on heat and mass transfer, emphasizing the importance of using the improved pressure coupling approach for accurate process modeling, especially at lower chamber pressures. The numerical results align well with experimental data, showing similar trends in vial temperatures and drying rates.

At a shelf temperature of  $-20$  °C, edge vials dry faster due to enhanced thermal radiation and additional heat transfer from the surrounding walls. This effect becomes more pronounced at  $+10$  °C, where edge vials exhibit approximately 20% shorter drying times. Despite these variations, the percent dry values remain within the confidence intervals of experimental measurements, although greater uncertainty is observed for center vials, likely due to differences in pore size resulting from uncontrolled nucleation.

The variations between 10R and 15R vials become particularly evident at lower chamber pressures (6 Pa). The smaller gap between the stopper and the shelf in 15R vials leads to a more significant pressure increase, which enhances heat transfer but also slows mass transfer, ultimately affecting drying times. At  $+10$  °C, 15R vials dry faster than 10R vials due to the increased pressure-induced heat transfer. In contrast, at  $-20$  °C, 15R vials exhibit longer drying times due to restricted sublimation flow. Furthermore, the product temperature of 15R

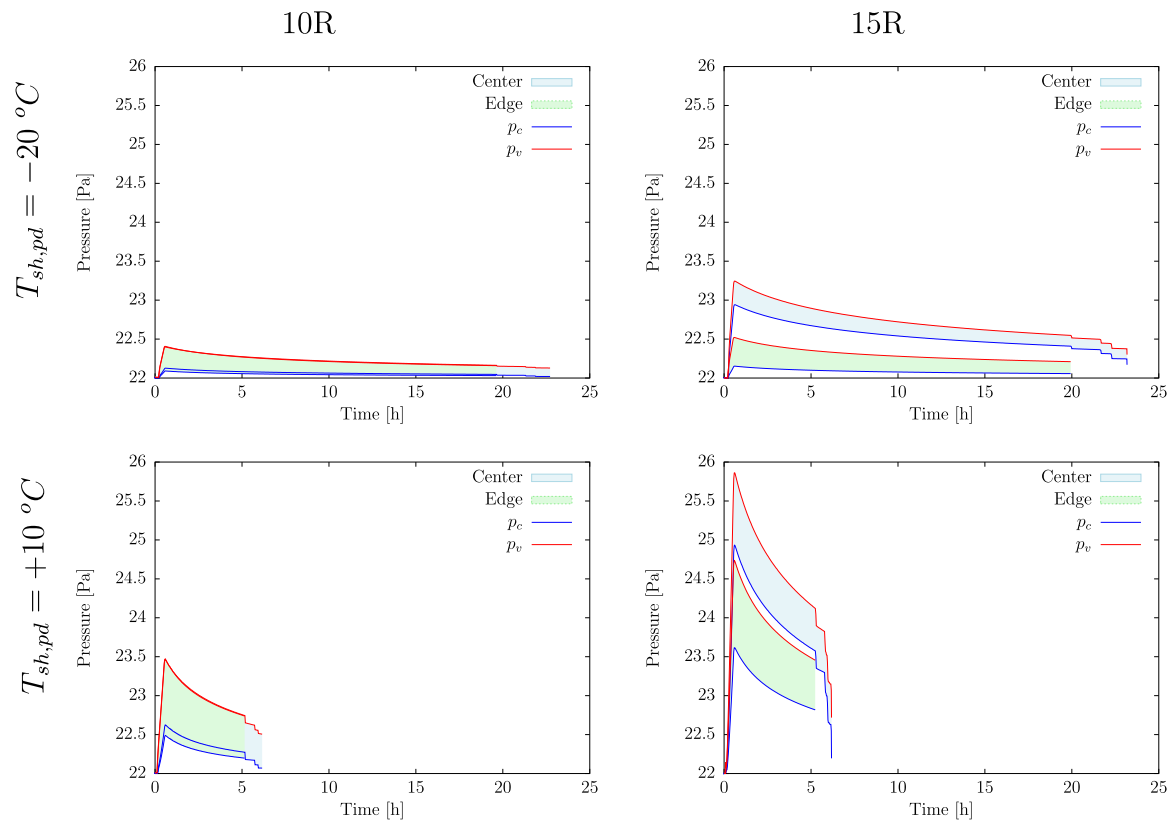


**Fig. 13.** Local pressure variations above the vials and in the headspace for 10R and 15R vials at a chamber pressure of 22 Pa. The pressure increase is minimal for 10R vials due to a larger gap across the stopper, while 15R vials show a higher pressure increase, especially at a shelf temperature of 10 °C, as a smaller gap restricts vapor flow.

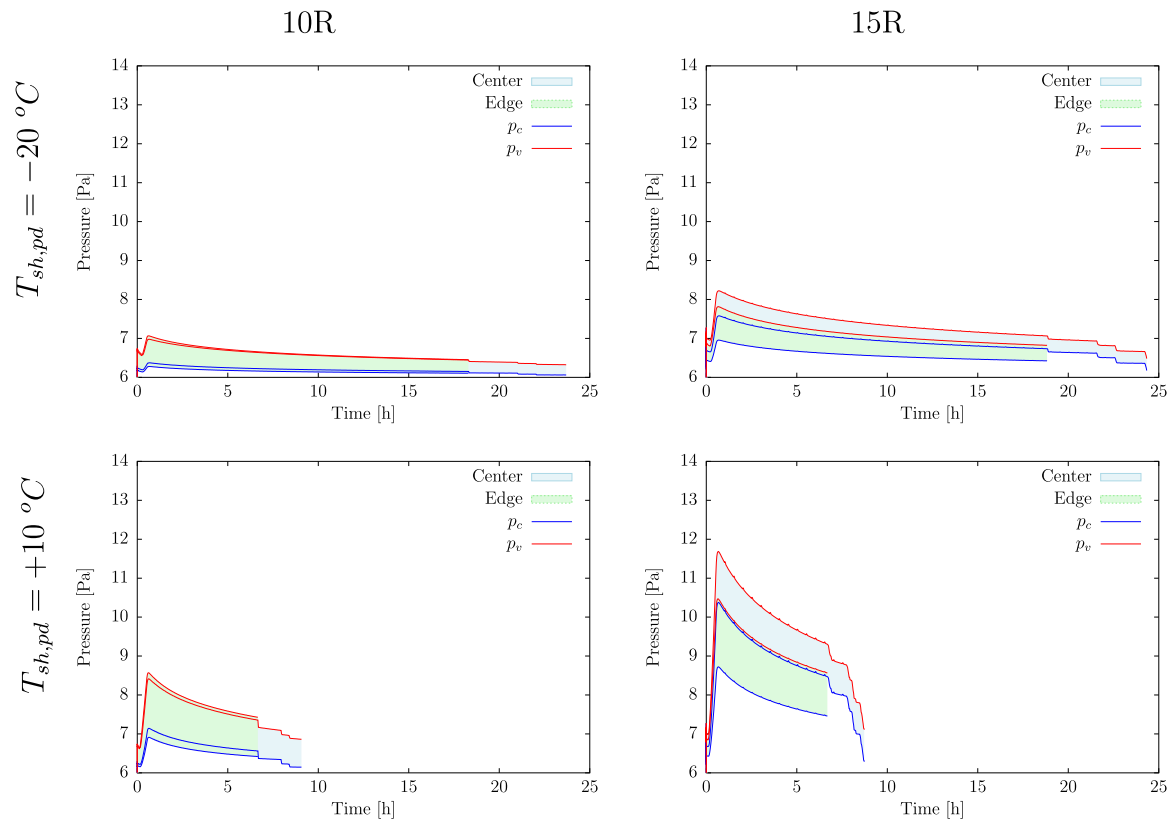


**Fig. 14.** Local pressure variations above the vials and in the headspace for 10R and 15R vials at a chamber pressure of 6 Pa. The pressure increase is more pronounced compared to a chamber pressure of 22 Pa, especially 15R vials show a higher pressure increase, which in turn is more pronounced at a shelf temperature of 10 °C, as a smaller gap restricts the vapor flow.

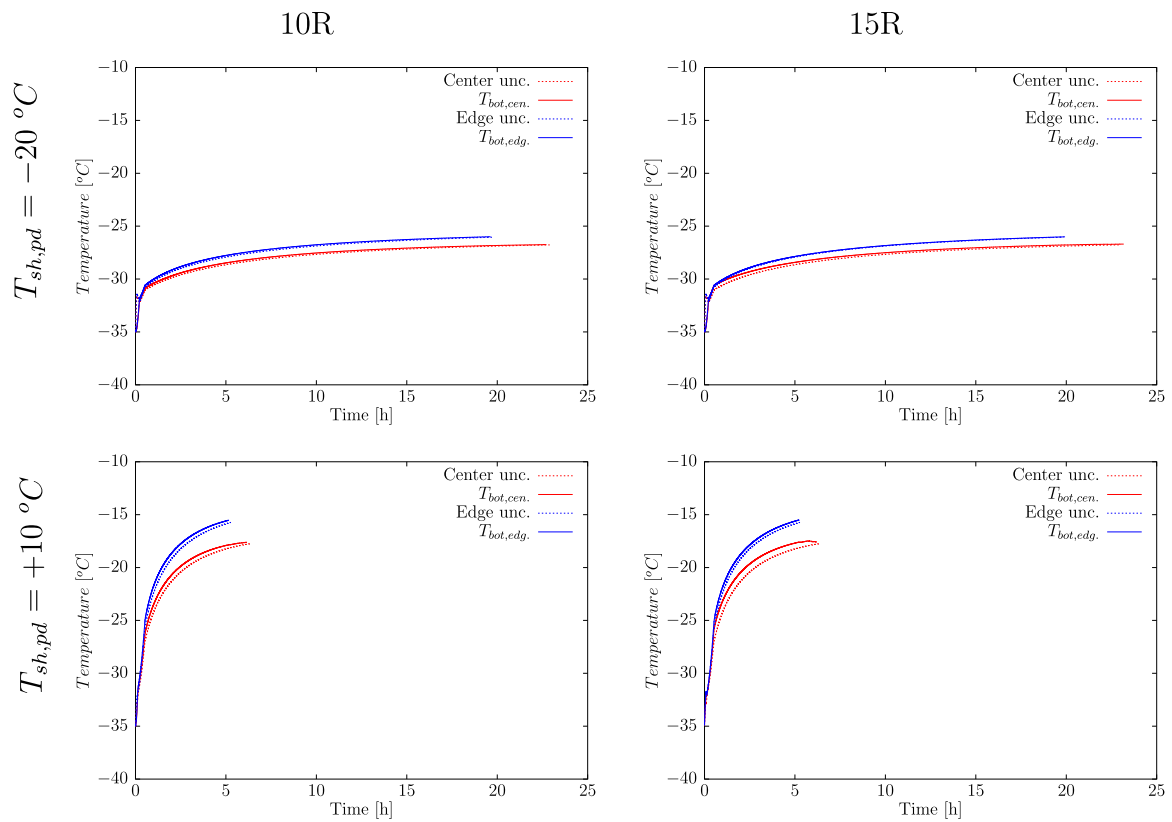


Fig. 15. Temperature profiles at the bottom of the product ( $T_{bot}$ ) for 10R and 15R vials at 22 Pa. The differences between the coupled and uncoupled solutions are minimal at a low shelf temperature of  $-20\text{ }^{\circ}\text{C}$ , but become more pronounced at a higher shelf temperature of  $10\text{ }^{\circ}\text{C}$ .

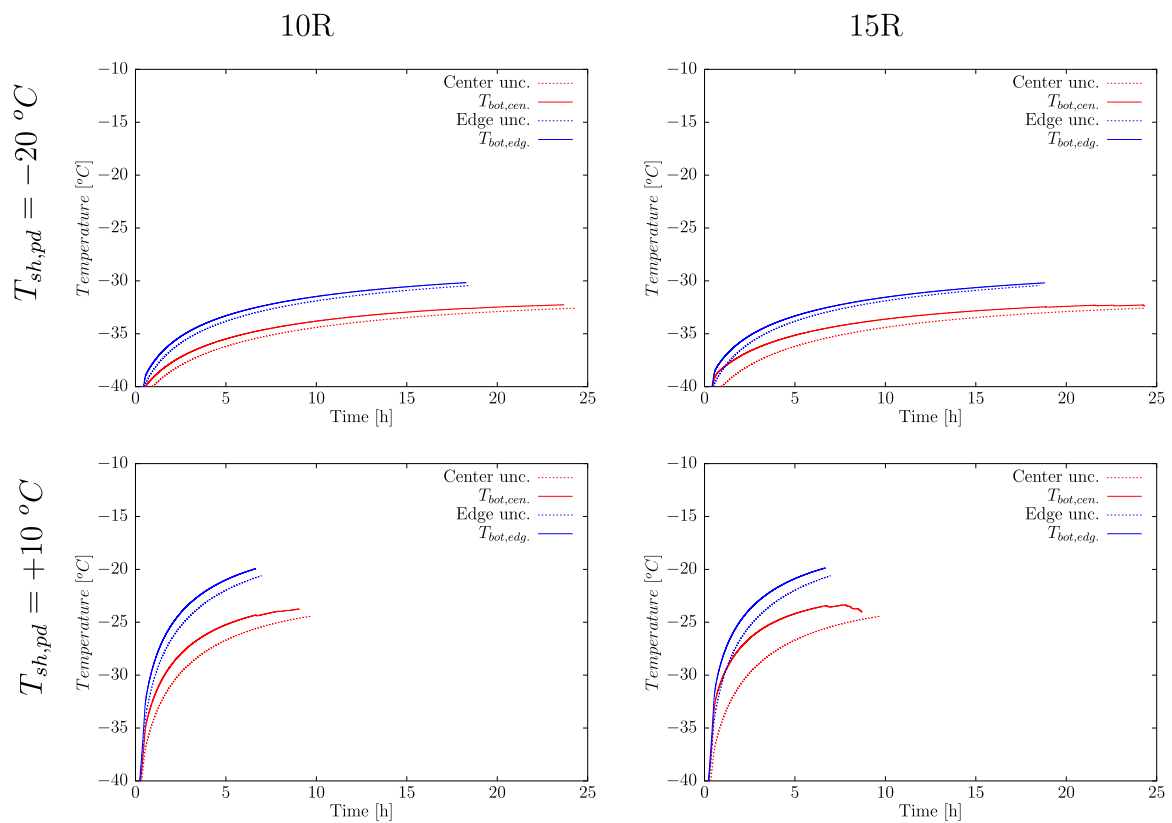
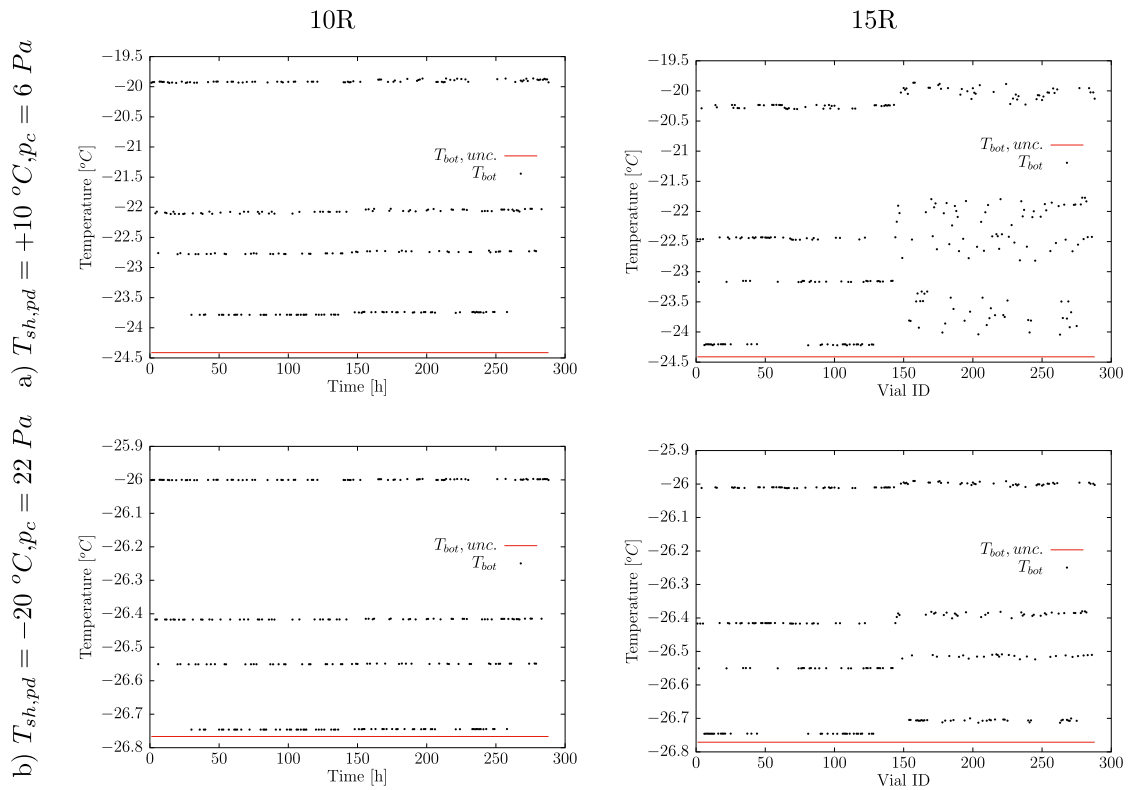


Fig. 16. Temperature profiles at the bottom of the product ( $T_{bot}$ ) for 10R and 15R vials at 6 Pa. At lower system pressure, the differences between coupled and uncoupled solutions are significantly larger, especially for the 15R due to increased local heat transfer.

**Table 3**

Maximum, minimum and average primary drying times (with standard deviation) for all vials in the freeze dryer (abbr. Both), bottomshelf (abbr. Bot) and the upper shelf (abbr. Up), comparing the results of the coupled and uncoupled (abbr. Unc.) models for 10R and 15R vials at chamber pressures of 6 and 22 Pa.

	Shelf	$T_{sh}$ [°C]	10R vial				15R vial			
			Max (h)	Min (h)	Avg (h)	SD ( $\sigma$ ) (h)	Max (h)	Min (h)	Avg (h)	SD ( $\sigma$ ) (h)
Pressure 6 Pa	Both	-20	23.72	18.29	21.05	2.07	24.70	18.83	21.71	2.15
		10	9.14	6.62	7.92	0.94	9.57	6.69	7.99	0.91
	Bot	-20	23.70	18.29	21.04	2.06	24.33	18.83	21.61	2.07
		10	9.09	6.62	7.90	0.93	8.72	6.69	7.74	0.70
	Up	-20	23.72	18.29	21.05	2.07	24.70	18.86	21.81	2.22
		10	9.14	6.65	7.94	0.95	9.57	6.87	8.25	1.02
	Unc.	-20	24.37				24.37			
		10	9.75				9.75			
Pressure 22 Pa	Both	-20	22.72	19.62	21.25	1.19	23.18	19.93	21.60	1.22
		10	6.17	5.15	5.69	0.39	6.32	5.24	5.78	0.38
	Bot	-20	22.72	19.62	21.25	1.19	23.18	19.93	21.63	1.24
		10	6.16	5.15	5.69	0.39	6.18	5.24	5.74	0.35
	Up	-20	22.72	19.62	21.25	1.19	23.08	19.93	21.57	1.21
		10	6.17	5.15	5.69	0.39	6.32	5.27	5.82	0.40
	Unc.	-20	22.94				22.94			
		10	6.32				6.32			



**Fig. 17.** Comparison of temperature at the bottom of the vial for all the vials inside of the freeze-dryer at the end of primary drying (a) shelf temperature of +10 °C and chamber pressure 6 Pa (b) shelf temperature of -20 °C at chamber pressure of 22 Pa for 10R vials (left) and 15R vials (right). The vials exhibit four discrete temperature levels due to the influence of packing factors.

vials is generally higher than that of 10R vials, reflecting the greater heat transfer effect associated with the increased local pressure. These findings highlight the importance of using a coupled model, especially in scenarios with small stopper-shelf gaps and lower chamber pressures, where pressure-induced effects on both heat and mass transfer play a crucial role in accurately predicting drying behavior and product temperature.

The coupled model shows a different drying behavior, especially at low pressure (6 Pa) and small stopper- shelf gaps, where the pressure build-up significantly influences the heat and mass transfer. At lower shelf temperatures (-20 °C), increased pressure for 10R vials led to

a reduction in drying time of 0.67 h (2.7%), whereas for 15R vials the coupling had only a minimal effect, reducing drying time by only 0.04 h (0.1%). At higher shelf temperatures (+10 °C), coupling reduced drying time by 0.66 h (6.7%) for 10R vials and 1.03 h (10.5%) for 15R vials, which is a more significant improvement. In addition, 15R vials on the bottom shelf at 6 Pa had a 3% longer drying time than 10R vials at -20 °C (24.33 h vs. 23.7 h), while the 15R vials dried 4% faster than 10R vials at +10 °C (8.72 h vs. 9.09 h). The data also showed improved uniformity of drying, particularly on the bottom shelf, at 6 Pa, with the bottom shelf deviation being 0.15 h (7%) less than the top shelf at -20 °C and 0.3 h (30.9%) less at +10 °C. These results

emphasize the importance of considering pressure effects, especially under conditions where the gap between the rubber stopper and shelf is small and the chamber pressure is 6 Pa or less. In conclusion, lower system pressure increases the temperature variation of the product between the fastest and the slowest drying vials, potentially impacting product stability. This highlights the need for pressure coupling in the model at lower chamber pressures to ensure accurate predictions and control of product temperature.

### Declaration of competing interest

The authors declare that they have no known competing financial interests or personal relationships that could have appeared to influence the work reported in this paper.

### Acknowledgments

The authors wish to thank the Slovenian Research and Innovation Agency (ARIS) for the financial support in the framework of the Programme P2-0196: Research in Power, Process and Environmental Engineering.

### Data availability

Data will be made available on request.

### References

- [1] G.-W.O. Peter Haseley, *Freeze-Drying*, third ed., WILEY-VCH, Weinheim, Germany, 2018, p. 437.
- [2] M. Pikal, M. Roy, S. Shah, Mass and heat transfer in vial freeze-drying of pharmaceuticals: Role of the vial, *J. Pharm. Sci.* 73 (9) (1984) 1224–1237.
- [3] J. Ravnik, I. Golobič, A. Sitar, M. Avanzo, Š. Irman, K. Kočevar, M. Cegnar, M. Zdravec, M. Ramšak, M. Hriberšek, Lyophilization model of mannitol water solution in a laboratory scale lyophilizer, *J. Drug Deliv. Sci. Technol.* 45 (2018) 28–38.
- [4] S. Zhai, H. Su, R. Taylor, N.K. Slater, Pure ice sublimation within vials in a laboratory lyophiliser; comparison of theory with experiment, *Chem. Eng. Sci.* 60 (4) (2005) 1167–1176.
- [5] M. Ramšak, J. Ravnik, M. Zdravec, M. Hriberšek, J. Iljaž, Freeze-drying modeling of vial using BEM, *Eng. Anal. Bound. Elem.* 77 (2017) 145–156.
- [6] L. Stratta, L.C. Capozzi, S. Franzino, R. Pisano, Economic analysis of a freeze-drying cycle, *Processes* 8 (11) (2020) 1–17.
- [7] Y. Liu, Y. Zhao, X. Feng, Exergy analysis for a freeze-drying process, *Appl. Therm. Eng.* 28 (7) (2008) 675–690.
- [8] M. Brülls, A. Rasmuson, Heat transfer in vial lyophilization, *Int. J. Pharm.* 246 (1) (2002) 1–16.
- [9] B. Scutellà, S. Passot, E. Bourlés, F. Fonseca, I.C. Tréléa, How vial geometry variability influences heat transfer and product temperature during freeze-drying, *J. Pharm. Sci.* 106 (3) (2017) 770–778.
- [10] J. Patricio Buceta, S. Passot, B. Scutellà, E. Bourlés, F. Fonseca, I.-C. Trelea, Use of 3D mathematical modelling to understand the heat transfer mechanisms during freeze-drying using high-throughput vials, *Appl. Therm. Eng.* 207 (2022) 118099.
- [11] T. Zhu, E.M. Moussa, M. Witting, D. Zhou, K. Sinha, M. Hirth, M. Gastens, S. Shang, N. Nere, S.C. Somashekar, A. Alexeenko, F. Jameel, Predictive models of lyophilization process for development, scale-up/tech transfer and manufacturing, *Eur. J. Pharmaceut. Biopharmaceut.* 128 (January) (2018) 363–378.
- [12] A. Ganguly, A.A. Alexeenko, S.G. Schultz, S.G. Kim, Freeze-drying simulation framework coupling product attributes and equipment capability: Toward accelerating process by equipment modifications, *Eur. J. Pharmaceut. Biopharmaceut.* 85 (2) (2013) 223–235.
- [13] S.M. Patel, S. Chaudhuri, M.J. Pikal, Choked flow and importance of mach I in freeze-drying process design, *Chem. Eng. Sci.* 65 (21) (2010) 5716–5727.
- [14] A.A. Barresi, R. Pisano, V. Rasetto, D. Fissore, D.L. Marchisio, Model-based monitoring and control of industrial freeze-drying processes: Effect of batch nonuniformity, *Dry. Technol.* 28 (5) (2010) 577–590.
- [15] A.A. Barresi, D.L. Marchisio, Computational fluid dynamics data for improving freeze-dryers design, *Data Brief* 19 (2018) 1181–1213.
- [16] A. Ganguly, S.L. Nail, A.A. Alexeenko, Rarefied gas dynamics aspects of pharmaceutical freeze-drying, *Vacuum* 86 (11) (2012) 1739–1747.
- [17] D.L. Marchisio, M. Galan, A.A. Barresi, Use of computational fluid dynamics for improving freeze-dryers design and process understanding. Part 2: Condenser duct and valve modelling, *Eur. J. Pharmaceut. Biopharmaceut.* 129 (January) (2018) 45–57.
- [18] B. Kamenik, M. Hriberšek, M. Zdravec, Determination of pressure resistance of a partially stoppered vial by using a coupled CFD-0D model of lyophilization, *Eur. J. Pharmaceut. Biopharmaceut.* 175 (2022) 53–64.
- [19] L. Stratta, R.P. and, The impact of the stopper position and geometry on the freeze-drying cycle of pharmaceutical products, *Dry. Technol.* 42 (13) (2024) 1999–2011.
- [20] A. Ganguly, A.A. Alexeenko, Modeling and measurements of water-vapor flow and icing at low pressures with application to pharmaceutical freeze-drying, *Int. J. Heat Mass Transfer* 55 (21–22) (2012) 5503–5513.
- [21] M. Petitti, A.A. Barresi, D.L. Marchisio, CFD modelling of condensers for freeze-drying processes, *Sadhana - Acad. Proc. Eng. Sci.* 38 (6) (2013) 1219–1239.
- [22] B. Kamenik, M. Hriberšek, M. Zdravec, Simulation of ice deposition in a freeze dryer condenser: A computational fluid dynamics study, *Appl. Therm. Eng.* 247 (2024) 123019.
- [23] V. Rasetto, D.L. Marchisio, D. Fissore, A.A. Barresi, On the use of a dual-scale model to improve understanding of a pharmaceutical freeze-drying process, *J. Pharm. Sci.* 99 (10) (2010) 4337–4350.
- [24] A.A. Barresi, V. Rasetto, D.L. Marchisio, Use of computational fluid dynamics for improving freeze-dryers design and process understanding. Part 1: Modelling the lyophilisation chamber, *Eur. J. Pharmaceut. Biopharmaceut.* 129 (January) (2018) 30–44.
- [25] J.M. Goldman, X. Chen, J.T. Register, V. Nesarikar, L. Iyer, Y. Wu, N. Mugheirbi, J. Rowe, Representative scale-down lyophilization cycle development using a seven-vial freeze-dryer (MicroFD), *J. Pharm. Sci.* 108 (2019) 1486–1495.
- [26] [www.kambic.com](http://www.kambic.com). Kambič, Laboratory and process equipment.
- [27] ANSYS Inc., ANSYS academic research, release 17.2, help system: Solver theory and multiphase flow theory, 2016, Accessed via ANSYS Fluent Help System.
- [28] J.J. Shu, J. Bin Melvin Teo, W. Kong Chan, Fluid velocity slip and temperature jump at a solid surface, *Appl. Mech. Rev.* 69 (2) (2017).
- [29] E.W. Lemmon, M.O. McLinden, D.G. Friend, *Thermophysical Properties of Fluid Systems*, National Institute of Standards and Technology, Gaithersburg MD, 2021.
- [30] J. Ravnik, M. Ramšak, M. Zdravec, B. Kamenik, M. Hriberšek, Experimental and stochastic analysis of lyophilisation, *Eur. J. Pharmaceut. Biopharmaceut.* 159 (2021) 108–122.
- [31] W. Mascarenhas, H. Akay, M. Pikal, A computational model for finite element analysis of the freeze-drying process, *Comput. Methods Appl. Mech. Engrg.* 148 (1) (1997) 105–124.
- [32] C. Song, J. Nam, A numerical study on freeze drying characteristics of cylindrical products with and without container, *Int. J. Transp. Phenom.* 7 (3) (2005) 241.
- [33] M. Ramšak, M. Zdravec, J. Ravnik, J. Iljaz, M. Avanzo, K. Kočevar, S. Irman, M. Cegnar, I. Golobic, A. Sitar, M. Hriberšek, Numerical and experimental modeling of lyophilization of lactose and mannitol water solutions in vials, *Comput. Therm. Sci.: An Int. J.* 12 (5) (2020) 401–415.
- [34] S. Rambhatla, M. Pikal, Heat and mass transfer scale-up issues during freeze-drying, I: Atypical radiation and the edge vial effect, *AAPS PharmSciTech* 4 (2003) E14.
- [35] B. Scutellà, A. Plana-Fattori, S. Passot, E. Bourlés, F. Fonseca, D. Flick, I.C. Tréléa, 3D mathematical modelling to understand atypical heat transfer observed in vial freeze-drying, *Appl. Therm. Eng.* 126 (2017) 226–236.
- [36] H. Gieseler, G. Lee, Effects of vial packing density on drying rate during freeze-drying of carbohydrates or a model protein measured using a vial-weighing technique, *Pharm. Res.* 25 (2) (2007) 302–312.
- [37] S. Hibler, C. Wagner, H. Gieseler, Vial freeze-drying, part 1: New insights into heat transfer characteristics of tubing and molded vials, *J. Pharm. Sci.* 101 (3) (2012) 1189–1201.
- [38] S. Ehlers, R. Schroeder, W. Friess, Trouble with the neighbor during freeze-drying: Rivalry about energy, *J. Pharm. Sci.* 110 (3) (2021) 1219–1226.
- [39] A. Matejčíková, P. Rajniak, Impact of packing density on primary drying rate, *Acta Chim. Slovaca* 13 (2) (2020) 30–37.